

# Emulation-based self-supervised SIF retrieval in the O<sub>2</sub>-A absorption band with HyPlant

Jim Buffat<sup>1,2</sup>, Miguel Pato<sup>3</sup>, Kevin Alonso<sup>4</sup>, Stefan Auer<sup>3</sup>, Emiliano Carmona<sup>3</sup>, Stefan Maier<sup>3</sup>, Rupert Müller<sup>3</sup>, Patrick Rademske<sup>2</sup>, Uwe Rascher<sup>2</sup>, and Hanno Scharr<sup>1</sup>

<sup>1</sup>Institute of Advanced Simulations, IAS-8: Data Analytics and Machine Learning, Forschungszentrum Jülich GmbH

<sup>2</sup>Institute of Bio-and Geosciences, Forschungszentrum Jülich GmbH

<sup>3</sup>Remote Sensing Technology Institute, German Aerospace Center (DLR)

<sup>4</sup>European Space Agency (ESA)

February 24, 2025

## Abstract

The retrieval of sun-induced fluorescence (SIF) from hyperspectral imagery requires accurate atmospheric compensation to correctly disentangle its small contribution to the at-sensor radiance from other confounding factors. In spectral fitting SIF retrieval approaches this compensation is estimated in a joint optimization of free variables when fitting the measured at-sensor signal. Due to the computational complexity of Radiative Transfer Models (RTMs) that satisfy the level of precision required for accurate SIF retrieval, fully joint estimations are practically inachieveable with exact physical simulation. We present in this contribution an emulator-based spectral fitting method neural network (EmSFMNN) approach integrating RTM emulation and self-supervised training for computationally efficient and accurate SIF retrieval in the O<sub>2</sub>-A absorption band of HyPlant imagery. In a validation study with in-situ top-of-canopy SIF measurements we find improved performance over traditional retrieval methods. Furthermore, we show that the model predicts plausible SIF emission in topographically variable terrain without scene-specific adaptations. Since EmSFMNN can be adapted to hyperspectral imaging sensors in a straightforward fashion, it may prove an interesting SIF retrieval method for other sensors on airborne and spaceborne platforms.

# Emulation-based self-supervised SIF retrieval in the O<sub>2</sub>-A absorption band with HyPlant

Jim Buffat<sup>a,d</sup>, Miguel Pato<sup>b</sup>, Kevin Alonso<sup>c</sup>, Stefan Auer<sup>b</sup>, Emiliano Carmona<sup>b</sup>, Stefan Maier<sup>b</sup>, Rupert Müller<sup>b</sup>, Patrick Rademske<sup>d</sup>, Uwe Rascher<sup>d</sup>, Hanno Scharr<sup>a</sup>

<sup>a</sup>*Forschungszentrum Jülich GmbH, Institute of Advanced Simulations, IAS-8: Data Analytics and Machine Learning, Jülich, Germany*

<sup>b</sup>*Remote Sensing Technology Institute, German Aerospace Center (DLR), Oberpfaffenhofen, Germany*

<sup>c</sup>*European Space Agency (ESA), Largo Galileo Galilei, Frascati 00044, Italy*

<sup>d</sup>*Forschungszentrum Jülich GmbH, Institute of Bio- and Geosciences, IBG-2: Plant Sciences, Jülich, Germany*

---

## Abstract

The retrieval of sun-induced fluorescence (SIF) from hyperspectral imagery requires accurate atmospheric compensation to correctly disentangle its small contribution to the at-sensor radiance from other confounding factors. In spectral fitting SIF retrieval approaches this compensation is estimated in a joint optimization of free variables when fitting the measured at-sensor signal. Due to the computational complexity of Radiative Transfer Models (RTMs) that satisfy the level of precision required for accurate SIF retrieval, fully joint estimations are practically inachievable with exact physical simulation. We present in this contribution an emulator-based spectral fitting method neural network (EmSFMNN) approach integrating RTM emulation and self-supervised training for computationally efficient and accurate SIF retrieval in the O<sub>2</sub>-A absorption band of HyPlant imagery. In a validation study with in-situ top-of-canopy SIF measurements we find improved performance over traditional retrieval methods. Furthermore, we show that the model predicts plausible SIF emission in topographically variable terrain without scene-specific adaptations. Since EmSFMNN can be adapted to hyperspectral imaging sensors in a straightforward fashion, it may prove an interesting SIF retrieval method for other sensors on airborne and spaceborne platforms.

*Keywords:* Sun-induced fluorescence, deep learning, hyperspectral sensors, radiative transfer modelling, spectral fitting methods

## 1. Introduction

Any application based on hyperspectral imagery of the earth’s surface acquired from remote platforms such as satellites, aircrafts or UAVs must consider the influence of the atmosphere at acquisition time. The atmospheric state has a confounding influence on the measured at-sensor radiance. In order to disentangle atmospheric effects from a physical surface variable of interest a firm understanding of the physical signal generation is necessary. Various atmospheric radiative transfer models (RTMs) have been developed (e.g. MODTRAN6 [1], 6S/6SV [2, 3], libRadTran [4]) to derive appropriate correction algorithms for these effects. In vegetation-related remote sensing it is crucial to couple such atmospheric models with leaf and soil optical properties, leaf-level energy fluxes [5, 6, 7, 8], and radiative transfer models in the canopy [9, 10] to enable accurate retrieval of biophysical parameters from remote sensing reflectances.

Similarly, the retrieval of sun-induced fluorescence (SIF) from hyperspectral imagery in atmospheric absorption bands relies heavily on accurate modelling of atmospheric radiative transfer and of sensor properties. The state of the atmosphere parameterized by its water vapour content, the type and density of aerosols at recording time as well as the pressure and temperature profiles along the optical path of the at-sensor signal modulate the radiance signal from which SIF is retrieved [11, 12, 13, 14]. Since in typical acquisition scenarios of hyperspectral at-sensor radiance for SIF retrieval no measurements are conducted to establish the signal contribution of the atmosphere during recording time, atmospheric variables must be estimated using RTMs in iterative processes. However, RTMs can often not be used directly in radiance-based estimation for individual pixels due to their computational cost. To reduce the retrieval dependency and the number of RTM simulations required to retrieve SIF from at-sensor radiance, a two-step procedure is assumed in various SIF retrieval methods as opposed to a joint estimation of surface, atmospheric and sensor related parameters. In a first step the atmosphere is characterized for a large number of pixels to derive the atmospheric transmittance with the help of an RTM. In a second step, these transmittance estimates are used to disentangle reflectance, fluorescence and possibly sensor miscalibrations commonly parametrized in center wavelength (CW) and full width at half maximum (FWHM) shifts. For example, [15, 16] derive a set of atmospheric transfer functions for single acquisitions using an RTM ’interrogation’ technique first introduced by [17]. Operationally, these

estimated transfer functions are finetuned to account for retrieval errors of atmospheric components, sensor noise, sensor mischaracterization and model inaccuracies by modifications of a procedure called *transmittance correction* [18, 19]. This type of finetuning of the atmospheric transfer functions is based on the presence of non-vegetated pixels that are not affected by fluorescence. The identification of non-vegetated soil pixels can be difficult, however, in many geographical areas and especially in observation set-ups resulting in pixel sizes larger than a few meters where *pure* pixels are rare.

The validity of constant atmospheric transfer across a large set of spatial pixels relies on the fact that in airborne imagery the auto-correlation distance of atmospheric factors influencing the at-sensor radiance is usually larger than the spatial extent of the prediction [20, 21]. In the case of airborne acquisitions this results usually in the use of a single RTM estimate per acquisition. In the case of spaceborne acquisitions with a much larger spatial footprint, as will be provided for example by the FLEX mission [22], this assumption is not satisfied and strategies to localize the atmospheric characterizations efficiently must be developed. In the context of atmospheric correction for accurate reflectance estimation [23] have for example recently demonstrated the use of local linear emulators for accurate and computationally efficient atmospheric correction.

Similarly to changing atmospheric conditions on spatial scales relevant to satellite observations, the strongly changing observational conditions in airborne observations of topographically variable terrain are a challenge for SIF retrieval algorithms based on spectral regions affected by O<sub>2</sub> absorption. The simplifying assumption of constant atmospheric transmittance is invalid in these cases since the resulting optical path differences cause large variance in the depth of these absorption features.

[24] has proposed a pathway to computationally efficient SIF retrieval in these observational conditions. A reconstruction based on a Principal Component Analysis (PCA) of atmospheric transfer functions is used to model the radiative transfer non-parametrically. The use of PCA reconstructions allows for localized radiative transfer estimations and, importantly, a joint retrieval of the transfer functions as well as surface and sensor related quantities impacting the at-sensor radiance. However, the PCA loadings are fitted non-parametrically since they are not formulated as functions of physical quantities (e.g., surface and sensor altitude, water vapour content, aerosol optical density) as would be the case with physically explicit RTM simulations. This (i) impedes the explanatory power of atmospheric estimates and

- (ii) does not allow for constraining the atmospheric estimates with known physical quantities.

In this work we propose the use of RTM emulation instead of the PCA-based radiative transfer formulation adopted in [24] to increase the physical accuracy of the Spectral Fitting Method Neural Network (SFMNN) in HyPlant FLUO data. Such an emulator-based SFMNN (EmSFMNN) approach has recently been validated for spaceborne DESIS data [25] in conjunction with a loss formulation similar to [24]. The authors find good agreement between their DESIS derived SIF product and HyPlant SIF estimates in a benchmark data set consisting of quasi-simultaneously recorded HyPlant and DESIS acquisitions highlighting the potential of this approach for hyperspectral sensors with improved spectral sampling intervals such as HyPlant FLUO and the FLORIS sensor onboard the ESA’s Earth Explorer Mission FLEX [22].

RTM emulation can be regarded as a computationally efficient approximation of the exact RTM computation by a function acting on the same input parameter space as its RTM counterpart [26]. The functional form of such emulators is not relevant a priori, but depends on the specifications of the application such as the required computational speed and reconstruction performance, the spectral range of the application and the input parameter dimensionality. In this contribution, we derive a polynomial emulator from a large simulation database replicating typical observational conditions and the sensor characterization of the hyperspectral imaging sensor system HyPlant as in [11, 27, 28]. We additionally extend this emulator to represent band-wise spectral miscalibration which is shown to be integral for accurate SIF retrieval in HyPlant data. The functional form of this emulator matches well the specific requirements of neural network training. The computational efficiency of its predictions and gradient computation are sufficient for training on large hyperspectral data bases. With this novel neural network approach to integrate a computationally efficient model of canopy level optical properties and atmospheric radiative transfer into a SIF retrieval scheme we are able for the first time to make use of a pixelwise geometrical parameterization for a joint estimation of SIF and reflectance in airborne SIF retrieval.

In this study, We focus on SIF retrieval of selected campaign data sets of the hyperspectral HyPlant sensor system [29, 30]. The sensor characteristics of HyPlant and size of HyPlant data sets are uniquely suited to develop and improve partly data-driven SIF retrieval algorithms such as ours. Since HyPlant data is often acquired during field campaigns featuring ground based

Data Set	Campaign	FLOX	$\Delta h$ [m]	$ \mathcal{D} $ [ $\times 10^3$ ]	Location
SEL-2018 (600 m)	SEL	✓	20	15 (5)	Selhausen, DE
WST-2019 (1500 m)	WST	✓	20	14 (5)	Braccagni, IT
CKA-2020 (600 m)	CKA	✓	20	10 (3)	Kl. Altendorf, DE
CKA-2020 (350 m)	CKA	✓	20	8 (2)	Kl. Altendorf, DE
CKA-2021 (350 m)	CKA	✓	20	4 (1)	Kl. Altendorf, DE
TOPO	SOP, HOE 600 m 2021 - 2023	—	300	11 (3)	Jülich, DE Hölstein, CH
PRE	PHY, HOE, TR32 CKA, SEL, SOP WST, NRS 350 - 1800 m 2018 - 2023	—	300	235 (38)	

Table 1: Data sets of compiled HyPlant acquisitions from different locations in the years 2018 - 2023. *Data Set* denotes a single compilation. With *Campaign* we denote the campaign identifier pointing to the used acquisitions according to the identified scheme outlined in the openly available HyData data set [30], with *FLOX* we denote the availability of simultaneous FLOX data, with  $\Delta h$  the maximum topographic variation over the compiled data set, with  $|\mathcal{D}|$  the data set size in terms of number of  $60 \times 60$  image crops. In parenthesis is reported the number of patches used for training.

SIF measurements, we are able to complement the present study with a direct comparison of SIF estimates of our approach with ground-based in-situ SIF estimates. However, we point out that while HyPlant is well suited to test the set-up presented in this work, EmSFMNN may be applied on data acquired by other airborne or spaceborne sensors. Its specific formulation is in fact well suited to cope with large existing hyperspectral data sets and continuous data streams of hyperspectral imaging sensors.

## 2. Data

### 2.1. Data quality provided by the HyPlant FLUO sensor

The HyPlant FLUO sensor [29] is the airborne demonstrator for the spaceborne FLEX satellite mission [22]. As such, it has been designed specifically for SIF retrieval in the atmospheric O<sub>2</sub>-A and O<sub>2</sub>-B absorption bands with a spectral sampling interval of 0.11 nm and a full width a half maximum (FWHM) of 0.25 nm. A large collection of hyperspectral HyPlant data sets

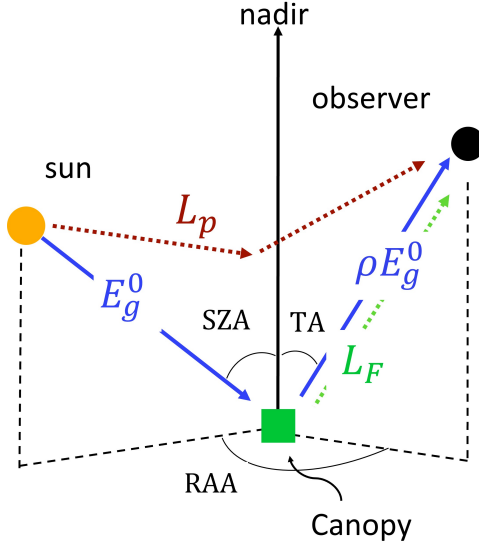


Figure 1: Geometrical set-up of the sun-observer geometry definitions in use.  $RAA$  denotes the relative azimuth angle,  $TA$  the tilt angle and  $SZA$  the sun zenith angle.

Specification		Range
Atmosphere	$H_2O$ [cm] $AOT_{550}$ []	0.3–3.0 0.02–0.30
Geometry	TA [°] SZA [°] RAA [°] $h_{\text{gnd}}$ [km] $h_{\text{agl}}$ [km]	0–25 20–55 0–180 0–0.760 0.2–2.86
Surface	$\rho_{740}$ [] $s$ [nm <sup>-1</sup> ] $e$ [] $F_{737}$ [*]	0.05–0.60 0–0.012 0–1 0–8
Sensor	$\Delta\lambda$ [nm] $\Delta\sigma$ [nm]	[-0.080, +0.080] [-0.040, +0.040]
Input dimensions		13
Number of bands		349
Number of samples		$6.3 \times 10^6$

Table 2: Specification of the ranges of all physical variables necessary for complete parametrization of the simulation tool.

\*:  $F_{737}$  is given in units of [mW/nm/sr/m<sup>2</sup>].

have been collected since 2014 [31, 32, 33, 34, 35, 36, 37] and are partly openly available [30]. In particular, yearly data sets since 2018 can be considered to be comparable across different campaigns due to their operationalized and standardized radiometric calibration and derivation of the geometric correction. Overall, the radiometric calibration is gauged at a mean relative uncertainty  $r_g$  of 3% [36] and the geolocalization reaches subpixel accuracy [29].

In this study, we make use of radiometrically corrected HyPlant FLUO acquisitions acquired in the years 2018 -2023 (cf. Tab. 1) in different flight campaigns, various locations and varying sun-observer geometries. The data set incorporates a large part of all available HyPlant FLUO acquisitions from this time period. We notably include acquisitions with strong topographic variation to train and to test the retrieval performance under these demanding conditions (cf. Sec. 4.4).

## 2.2. Simulation of *HyPlant* at-sensor radiance

The emulator utilized in this work is based on the polynomial emulator described in [27, 28] derived from a simulation tool generating single pixel at-sensor radiance [11]. It uses MODTRAN6 to model radiative transfer through the atmosphere and assumes simple parametric models for surface reflectance and fluorescence emission in the spectral range around the O<sub>2</sub>-A oxygen absorption band. The parameters of the simulator have been chosen according to an extensive sensitivity study performed in [11]. We fixed the ranges of the resulting 13 parameters such that they cover the empirical distributions found in the *HyPlant* acquisitions used in this work (cf. Tab. 2). Appropriate ranges for the geometric parameters sensor altitude above ground level  $h_{\text{agl}}$ , ground altitude  $h_{\text{gnd}}$ , relative azimuth angle RAA and tilt angle TA could be established exactly from metadata provided with *HyPlant* data taking account of its precise orientation. The ranges for the surface parameters and for the sensor characterization also were adopted directly from preparatory work in [27, 28]. The parameterization of a simple quadratic reflectance model implemented in the simulation tool was chosen according to an analysis of vegetation and soil reflectance spectra of the DUAL hemispherical-directional reflectance product that is computed operationally for all *HyPlant* acquisitions. Equally, we modelled fluorescence emission in the O<sub>2</sub>-A band spectral region with a Gaussian with fixed mean ( $\mu = 737$  nm), fixed standard deviation ( $\sigma_f = 20$  nm) and a free amplitude  $F_{737}$ . The ranges regarding the sensor characterization parameterized by center wavelength shifts  $\Delta\lambda$  and FWHM shifts  $\Delta\sigma$  were derived from in-flight data. Due to lacking simultaneous measurements, which would have allowed an estimate of the ranges of the atmospheric parameters aerosol optical thickness  $\text{AOT}_{550}$  and water vapour density  $\text{H}_2\text{O}$ , these ranges were chosen such that they covered all possible atmospheric states in which *HyPlant* campaigns are operated (cloud-free weather conditions in mid-latitude regions in summer).

We sampled the parameter ranges in Tab. 2 with different sampling strategies for training and validation data set to derive an emulator as outlined in [27, 28]. Importantly, the input parameters  $p$  were sampled independently. Since the parametric models for the spectral shapes of the reflectance and fluorescence implemented in the simulation tool were completely independent as well, we prevented our retrieval method to incorporate cross-correlations between fitted parameters a-priori as this would undermine the purely physical approach followed in this work.

### 2.3. *In-situ SIF validation data*

For a subset of the HyPlant acquisitions used in this work in-situ measurements of SIF are available (cf. Tab. 1). All in-situ measurements were derived with the Improved Fraunhofer Line Discrimination Method (iFLD) [38] from radiance point measurements and solar irradiance recordings of the hyperspectral FLOX device (Fluorescence Box, JB-Hyperspectral Devices GmbH, Duesseldorf, Germany). In the case of the FLOX measurement series matching with CKA-2020 HyPlant acquisitions, the in-situ measurements were taken in four different locations by four different devices. One FLOX was placed in an agricultural oat field and three others in wheat fields. For the validation, we have aggregated the time series and did not differentiate between the different FLOX devices. The localization of those FLOX systems was improved with an exact GPS RTK measurement at each of the devices. In case of the in-situ measurements matching the SEL-2018 HyPlant acquisitions, a single mobile FLOX device was used in agricultural fields of sugar beet and wheat.

FLOX measurements falling within a 5 minutes to the acquisition time of HyPlant were considered. We selected only FLOX measurements flagged as having high radiometric stability ( $< 1\%$  difference in solar irradiance over the course of the measurement) in order to exclude measurements affected by cloud and haze. Since HyPlant campaigns are only conducted in optimal weather conditions, no measurements had to be excluded. In the case of multiple measurements within this time window matching a single acquisition, we averaged the FLOX iFLD SIF estimate to compare with HyPlant derived SIF estimates. In order to account for localization errors as well as the field of view we compared HyPlant pixels within a 2 m radius around the measurement location. The temporal and spatial variance resulting from the time windowing and spatial localization buffer were used as proxies for uncertainty estimates in the performance calculations.

## 3. Methods

### 3.1. *Simulation Tool*

The simulation tool utilized in this work [11, 27, 28] uses MODTRAN6 to simulate the HyPlant at-sensor radiance in a spectral range covering the

O<sub>2</sub>-A absorption band (740 - 780 nm) according to the model

$$L_s(\mathbf{p}) = \left( L_p + \frac{E_g^0 \rho T^\uparrow}{\pi(1 - \rho S)} + L_F T^\uparrow \right) (\mathbf{p}) \quad (1)$$

as a function of the parameters  $\mathbf{p}$  (as defined in Tab. 2) where  $L_p$  is the path radiance,  $E_g^0$  is the global solar irradiance on the ground,  $T^\uparrow$  is the total transmission coefficient from surface to sensor (direct and diffuse components,  $T^\uparrow = T_{\text{dir}}^\uparrow + T_{\text{dif}}^\uparrow$ ),  $L_F$  is the top-of-canopy fluorescence emission modelled as a Gaussian with fixed variance and amplitude  $F_{737}$ ,  $S$  is the spherical albedo of the atmosphere,  $\rho$  is the hemispherical-directional reflectance modelled as a 2<sup>nd</sup> order polynomial with offset  $\rho_{740}$ , slope  $s$  and curvature  $e$ , H<sub>2</sub>O denotes the columnar water vapour content, AOT<sub>550</sub> the aerosol optical thickness, TA the viewing angle, SZA the solar zenith angle, RAA the relative azimuth angle between observation and irradiance directions,  $h_{\text{gnd}}$  the topographic height above sea level,  $h_{\text{agl}}$  the sensor height above ground level and  $\Delta\lambda$  and  $\Delta\sigma$  the scalar shifts in the center wavelength and full width at half maximum (FWHM). In order to be consistent with in-situ reference fluorescence estimates, we report SIF<sub>760</sub> instead of  $F_{737}$  in all validation and analysis sections which we define as the functional value of the modelled fluorescence emission at 760 nm. The simulations have been conducted with an atmospheric model corresponding to the MODTRAN *mid-latitude summer* model. Thus, we have disregarded changes in the atmospheric pressure profile that might be caused by changing meteorology or topography. Finally, as in [28, 27], we densely sample the parameter space spanned by the parameter ranges in Tab. 2 and run a total of  $6.3 \times 10^6$  simulations.

### 3.2. Definition of the polynomial emulator

Emulation of a hyperspectral simulator  $L_s(\mathbf{p}) : \mathbb{R}^M \rightarrow \mathbb{R}^\Lambda$  from physical parameters  $\mathbf{p} \in \mathbb{R}^M$  by an emulator  $e$  is ultimately a regression problem where we derive a function  $e : \mathbb{R}^M \rightarrow \mathbb{R}^\Lambda$  that reproduces as closely as possible the simulator  $L_s$  at reduced computational cost. In practice, there is a trade-off between reducing the residual between simulator and emulator on the one hand and reducing the computational cost of  $e$  on the other for any non-trivial simulator  $L_s$ . Since the emulator is used during the training of a neural network, we require additionally that its gradient computation is efficient and preferably can be integrated easily in common programming frameworks for

deep learning. The polynomial emulator investigated by [27, 28] fulfills these requirements. It is defined as the polynomial function of  $d^{th}$  order

$$e_d(\mathbf{p} \mid \mathbf{a}_{\mathcal{K}^d}) = \sum_{\mathbf{k} \in \mathcal{K}^d} p_1^{k_0} \dots p_M^{k_M} \mathbf{a}_{\mathbf{k}}, \quad (2)$$

over the parameters  $\mathbf{p}$ , where  $\mathbf{a}_{\mathbf{k}} \in \mathbb{R}^{\Lambda}$  and where the set of polynomial features is defined as

$$\mathcal{K}^d = \left\{ \mathbf{k} \in \mathbb{N}^M : \sum_{1 \leq i \leq M} k_i \leq d \right\} \quad (3)$$

We train the emulator weights  $\mathbf{a}_{\mathbf{k}}$  in a least-squares optimization with a training subset of the data points partitioned from the total simulation data set as in [27, 28].

### 3.3. Emulation of a wavelength dependent sensor characterization

The simulation data base is created for scalar shifts  $\Delta\lambda$  and  $\Delta\sigma$ , i.e. simulated spectra  $s(\mathbf{p}) \in \mathbb{R}^{\Lambda}$  will suffer the same simulated sensor miscalibration in all wavelengths  $\lambda \in \Lambda$ . In a realistic sensor model, CW and FWHM shifts are, however, functions of the wavelength such that we ought to find an emulator with dependency on shifts  $\Delta\lambda \in \mathbb{R}^{\Lambda}$  and  $\Delta\sigma \in \mathbb{R}^{\Lambda}$  in addition to the other input parameters  $\tilde{\mathbf{p}}$ . We assume that there is no cross dependency of the shifts either in the measured at-sensor radiance  $L$  or the simulator  $L_s$ , i.e.

$$\forall i \neq k : \frac{dL_i}{dv_k} = \frac{d(L_s)_i(\tilde{\mathbf{p}}, \Delta\lambda, \Delta\sigma)}{dv_k} = 0, \quad v \in \{\Delta\lambda, \Delta\sigma\}. \quad (4)$$

In this case a naive approach to extend the emulator could be achieved by rewriting

$$e_d^{\Lambda}(\tilde{\mathbf{p}}, \Delta\lambda, \Delta\sigma) = (e_d(\lambda_i \mid \tilde{\mathbf{p}}, \Delta\sigma_i, \Delta\lambda_i))_{0 \leq i \leq \Lambda} \quad (5)$$

As the simulation data base covers a large number of spectral bands ( $\Lambda = 349$ ) such an approach results in a significant increase in computation time for a single spectrum since the emulator would need to be run  $\Lambda$  times for a single emulated spectrum. We therefore adopt an approximation. We derive a multiplicative correction factor

$$m(\lambda_i \mid \Delta\lambda, \Delta\sigma) = \mathbb{E}[w(\lambda_i \mid \tilde{\mathbf{p}}, \Delta\lambda_i, \Delta\sigma_i)] \quad (6)$$

$$= \mathbb{E}\left[\frac{e_d(\lambda_i \mid \tilde{\mathbf{p}}, \Delta\lambda_i, \Delta\sigma_i)}{e_d(\lambda_i \mid \tilde{\mathbf{p}}, \Delta\lambda_i = \Delta\sigma_i = 0)}\right] \quad (7)$$

Module	Parameters		
Encoder $e_{\text{in}}$	$Dim.$	(2e3, 2e3, 1e3, 5e2, 5e2, 1e2, 1e2, 1e2, 50)	
	$Reps.$	(3, 3, 3, 3, 3, 3, 3, 1, 1)	
	$D_p$	(0.05, 0.05, 0.01, 0.01, 0.005, 0.0)	
Decoder $d_v$	$Dim.$	(1e2, 50, 50, 50, 10)	
	$Reps.$	(3, 2, 2, 1)	
	$D_p$	(0.05, 0.05, 0.01, 0.01, 0.005, 0.0)	
Sensor charact. g	$Dim.$	(1e2, 50, 50, 50, 10)	
	$Reps.$	(3, 2, 2, 1)	
	$D_p$	(0.05, 0.05, 0.01, 0.01, 0.005, 0.0)	

Table 3: Dimensionalities for different modules in the EmSFMNN architecture (cf. Fig. 2). Elements in a tuple denote an architecture parameter for a single sublayer in a module.  $Reps.$  denotes the number of repetitions of linear layers in a sublayer,  $D_p$  denotes the dropout rate of the output of the sublayer. For a more detailed exposition of the module architecture we refer to [24].

where the expectation is calculated by sampling randomly over the parameter distribution in the input parameter space. As we will show below, the variance over this distribution is very small, such that we can write

$$\tilde{e}_d(\lambda_i | \tilde{\mathbf{p}}, \Delta\lambda, \Delta\sigma) \approx m(\lambda_i | \Delta\lambda, \Delta\sigma) \cdot e_d(\lambda_i | \tilde{\mathbf{p}}, \Delta\lambda_i = \Delta\sigma_i = 0) \quad (8)$$

### 3.4. Neural Network Architecture

We integrate a fourth-order emulator  $\tilde{e}_4$  of the radiative transfer in Eq. 1 with a self-supervised neural network. We construct a neural network acting on fixed size excerpts of HyPlant imagery ( $60 \times 60$ ) that we will refer to as *patches*. The network architecture is defined as in SFMNN [24] and similarly to a DESIS EmSFMNN implementation [25] (cf. Fig. 2) as a Multilayer Perceptron (MLP) encoder-decoder set-up. The network is trained to predict all parameters  $\mathbf{p}$  of the RTM model in Eq. 1 that cannot be inferred from metadata or geometrical recordings, i.e. all parameters in Tab. 2 except parameters of the group *Geometry*.

The encoder  $e_{\text{in}}$  and decoder modules  $d_v$  in this network are constructed as MLPs with residual links and have the dimensionalities given in Tab. 3. The decoders are tasked with disentangling the latent space spanned by the encoder to the physical parameters  $\tilde{\mathbf{p}}$  parameterizing the radiative transfer

model underlying the simulation tool and, thus, the emulator. We define two decoders  $d_v$ : for the reflectance and fluorescence related parameters predicted for each pixel and for the atmospheric parameters predicted for each patch. These two decoder modules are implemented identically with the exception of a final spatial mean reduction before the emulator layer in the case of the patchwise predictor. As in SFMNN, we differentiate between pixel-wise and patch-wise prediction based on the fact that atmospheric parameters (AOT and  $H_2O$ ) have an autocorrelation that typically exceeds the physical patch size such that a single atmospheric estimate per patch can be assumed to lead to sufficiently precise approximations.

The estimation of sensor shifts  $\Delta\lambda$  and  $\Delta\sigma$  is implemented differently. We assume that we can fit these shifts as a function of the sensor state at acquisition time and the across-track sensor position alone without any spectral input. This assumption is implemented in the architecture by estimating the sensor shifts only from an arbitrarily defined acquisition identifier  $\mathbf{u} \in \mathbb{R}^U$  that represents the sensor state and the across-track position  $x_1$ . At the start of the training we randomly instantiate these identifiers  $\mathbf{u}$  of fixed dimensionality ( $U = 8$ ) for each acquisition in the training data set and include them as learnable parameters in the optimization. The MLP module  $g$  predicts shifts  $\Delta\lambda$  and  $\Delta\sigma$  for each wavelength ( $\Lambda = 349$ ) at across-track positions  $x_1$  from pixelwise concatenations of the identifier vectors  $\mathbf{u}$  and a positional encoding of  $x_1$  [39].

An important characteristic of this particular set-up consists in the physically coherent separation of inputs and the differentiation of output dimensions for individual parameters. For example, all reflectance parameters ( $\rho_{740}$ ,  $s$ ,  $e$ ) and the fluorescence emission amplitude  $F_{737}$  are estimated for each pixel from the radiance data and geometrical information  $\nu_{\text{geo}}$ , but without providing the acquisition identifier  $u$  since the decoders to those parameters by definition do not depend on sensor characteristics or acquisition dependent changes. Similarly, atmospheric parameters are estimated from radiance and  $\nu_{\text{geo}}$  alone, but, differently to the surface parameters, only per patch as we assume negligible variance of these parameters over small spatial distances. The sensor characterization  $\Delta\lambda$  and  $\Delta\sigma$  on the other hand is uniquely estimated from the acquisition identifier  $u$  for individual across-track positions  $x_1$  since it is driven by factors that are identical across single acquisitions. Both input separation and differentiation in output dimensionality constrain the network optimization architecturally with prior knowledge of the physical processes and sensor design at play. On the other hand, we implicitly con-

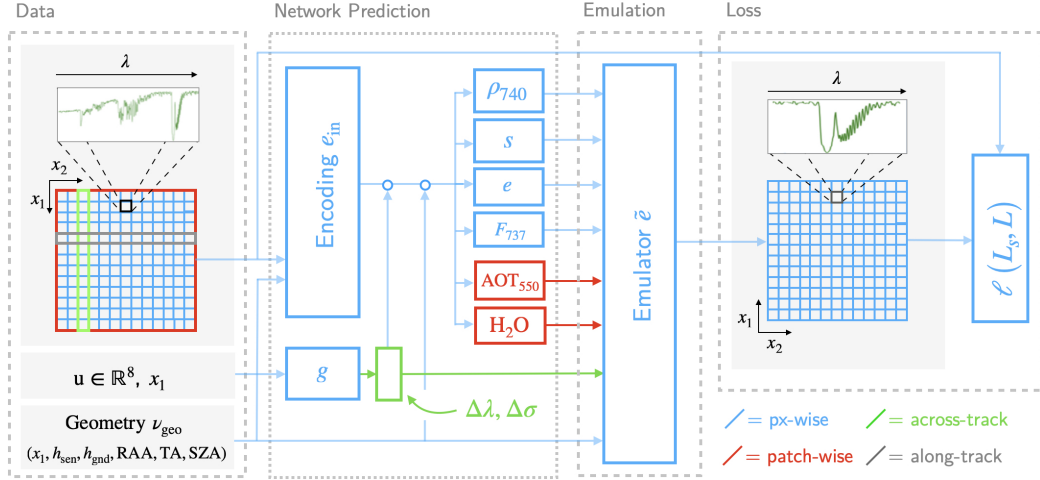


Figure 2: Outline of the architecture and emulator integration of the SFMNN used in this work. Dimensions of the encoder  $e_{in}$ , the decoders for variables  $\rho_{740}$ ,  $s$ ,  $e$ ,  $F_{737}$ ,  $AOT_{550}$  and  $H_2O$  and the sensor characterization  $g$  are given in Tab. 3.

strain the network by enforcing physically accurate solutions of the radiative transfer equation Eq. 1 given a particular parametrization  $\tilde{\mathbf{p}}$ . Differently to the simplified four-stream model used in SFMNN to model at-sensor radiances, the emulator  $\tilde{e}$  allows for pixel-wise parameterization of the radiative transfer formulation with known geometrical variables. This is a significant improvement over SFMNN’s formulation as the solution space of the network can be constrained very precisely in a pixel-wise fashion.

### 3.5. Loss formulation

The loss used in this set-up is adapted from the loss used in [24]. It consists of a batchwise mean squared reconstruction error complemented by two regularizers. Given the input radiance spectra  $L_{HyP}$  as measured by HyPlant and matching geometrical meta data  $\nu_{geo}$  (flight  $h_{sen}$  and ground altitude  $h_{gnd}$ , relative azimuth RAA, tilt angle TA and solar zenith angle SZA) we train the network  $n$  to minimize

$$\ell(L_{HyP}, \hat{L}_{HyP}) = \left\langle \left( L_{HyP} - \hat{L}_{HyP} \right)^2 \right\rangle_{\lambda, x} + \gamma_f \ell_f + \gamma_N \ell_{NDVI}, \quad (9)$$

where  $L_{HyP}$  is the measured at-sensor radiance in the spectral window  $\mathcal{W}$  and

$$\hat{L}_{HyP} = \tilde{e}(\tilde{\mathbf{p}}, \Delta\lambda, \Delta\sigma, \nu_{geo}) \quad (10)$$

denotes the network prediction with predicted  $\tilde{\mathbf{p}}$ ,  $\Delta\lambda$  and  $\Delta\sigma$ .  $\langle \dots \rangle_{x,\lambda}$  denotes the spatial and spectral mean over the patches included in a batch. Throughout all experiments in this work we have fixed the regularizer weights  $\gamma_f = 1$  and  $\gamma_{\text{NDVI}} = 10$ . These weights were established as they have shown satisfactory results in preliminary tests on the CKA-2020 (600 m) data set (cf. Tab. 1).

The fluorescence regularization

$$\ell_f = \left\langle \sum_{\lambda \in \mathcal{W}} w_\lambda \left( L_{\text{HyP}}(\lambda) - \hat{L}_{\text{HyP}}(\lambda) \right)^2 \right\rangle_x \Big|_{\delta p_i = 0, p_i \neq F_{737}} \quad (11)$$

boosts the contribution of reconstruction residuals according to a SNR-based weighting  $w_\lambda$  that accounts for the spectral distribution of typical fluorescence emission. This weighting is derived as the Moore-Penrose solution to a linearized retrieval problem with known reflectance and atmospheric parameters [24]. We thus restrict the gradient contribution of this loss term to affect only the fluorescence decoder (i.e. network weights uniquely related to parameters  $p_i \neq F_{737}$ , i.e. reflectance, atmospheric and sensor parameters, are not affected by this term). The physiologically motivated regularizer

$$\ell_{\text{NDVI}} = \left\langle \hat{f} \cdot \delta(\text{NDVI} < \tau) \right\rangle_x \quad (12)$$

ensures that the fluorescence estimate  $f$  vanishes in pixels with very low green vegetation, i.e. in pixels with a low Normalized Difference Vegetation Index (NDVI). To identify these pixels, we set a threshold  $\tau = 0.15$  on an approximate NDVI product derived from the radiance  $L_{\text{HyP}}$ .

### 3.6. Training set-up

The training of the EmSFMNN SIF predictors takes place in two steps. We first train a backbone on the PRE HyPlant data set (cf. Tab. 1). This backbone is used as the initialization to all EmSFMNN instances that are trained for individual data sets in the second step. Finetuning of PRE aims at adjusting the network (1) to the data set specific radiance calibration, (2) to train the acquisition specific identifiers  $u$  that determine the estimated shifts  $\Delta\lambda$  and  $\Delta\sigma$  and (3) to train in the specific parameter ranges covered differently in the various data sets (e.g. TOPO exhibiting larger variation of  $h_{\text{agl}}$ ). During the finetuning step, the encoder  $e_{\text{in}}$  is fixed and only the decoders  $d_v$ , the identifiers  $u$  and the sensor characterization  $g$  are trained.

As the identifiers  $u$  are not estimated from the radiance data but rather implicitly as a result of the architectural constraint in each acquisition, there is no generalization property of this part of the network. Thus, in order to get meaningful shift predictions, a finetuning is thus necessary. When EmSFMNN instances are applied to data sets for which they were not finetuned, arbitrary identifiers  $u$  are selected from the set of finetuned  $u$ . This procedure results in larger reconstruction errors than would have been possible with a finetuning of  $u$  but it doesn't necessarily affect the fluorescence estimate negatively. The spectral reconstruction window  $\mathcal{W}$  was fixed to cover 750 - 770 nm.

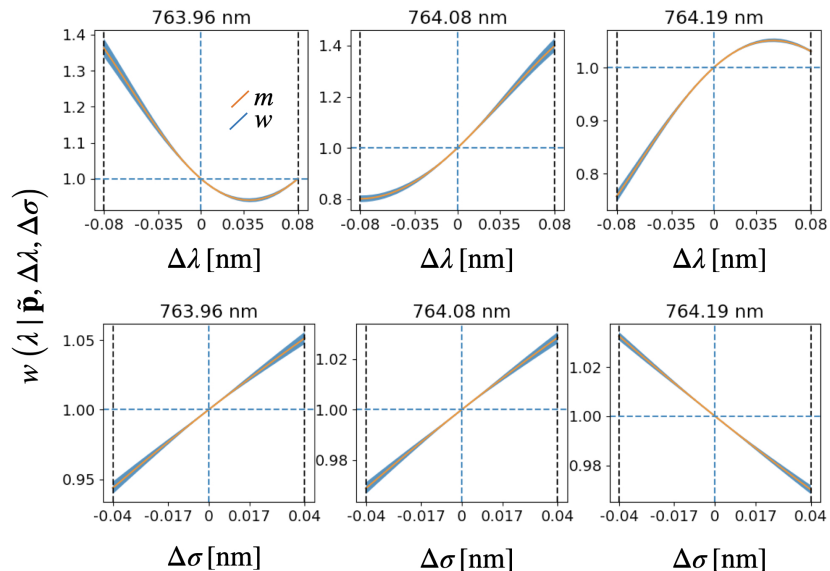


Figure 3: Multiplicative change  $w$  of  $e_4$  under variable sensor shifts ( $\Delta\lambda$  and  $\Delta\sigma$ ) in three selected wavelengths. In blue is plotted the standard deviation of  $w$  (as defined in Eq. 6) over the distribution of randomly sampled emulator parameter configurations  $\mathbf{p}$ . The fitted mean used as multiplicative correction  $m$  (see Eq. 6) is plotted in orange.

## 4. Results

### 4.1. Training of emulator extension for bandwise spectral shifts

We have derived a polynomial emulator of 4<sup>th</sup> order of HyPlant at-sensor radiance  $e_4$  for the parameter ranges given in Tab. 2. In order to allow for

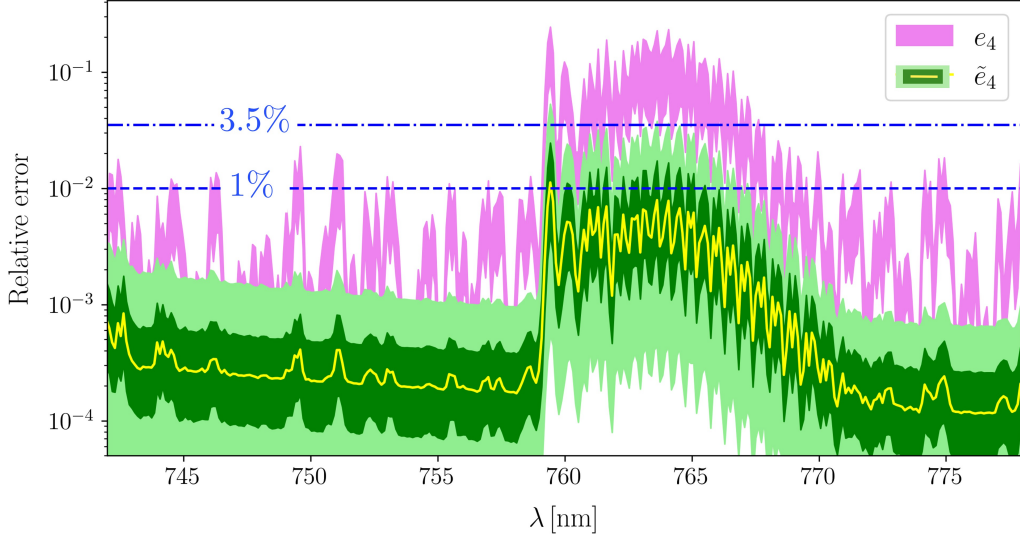


Figure 4: Relative errors of the approximate emulator  $\tilde{e}_4$  (green/yellow) and scalar shift emulator  $e_4$  (pink) with respect to the accurate  $e_4^\Lambda$  emulator. In the case of  $e_4$  we set  $\Delta\lambda = \Delta\sigma = 0$ . The 25 - 75 % percentile range is plotted in dark green, the 5 - 95 % percentile range in light green, the mean in yellow. Pink denotes the 25 - 75 % percentile range.

efficient training we then have implemented the emulator extension for wavelength dependent shifts  $\tilde{e}_4$  based on the polynomial emulator  $e_4$  which acts only on scalar shifts as outlined in Sec. 3.2. To this end, we have computed the multiplicative factor  $m$  as the expectation in Eq. 6. To compute the distribution, we uniformly sampled a large number of parameter combinations  $\mathbf{p}$  and sensor shifts  $\Delta\lambda$  and  $\Delta\sigma$  in the input space spanned by the individual parameter ranges.

We found the standard deviations of  $w$  to be bounded by 3.5% under CW shifts and 0.06% by FWHM shifts which we regarded as sufficiently small to approximate it by its mean  $m$  (cf. Fig. 3). Subsequently, we fitted a 5<sup>th</sup> order polynomial to the derived  $m$  to gain a multiplicative factor defined on the whole input parameter space discarding the need for interpolation during prediction. The dimension of this polynomial was required to be just large enough to fit  $m$  well. The use of  $\tilde{e}_4$  leads to a significant time reduction as compared to  $e_4^\Lambda$  (cf. Tab. 4).

In order to evaluate the accuracy of  $\tilde{e}_4$  we compared it to  $e_4^\Lambda$  on a uniformly sampled test set. While  $e_4^\Lambda$  takes significantly longer to compute, its accuracy

with respect to the RTM is as high as the emulator itself since it essentially computes the emulator in a bandwise fashion. In Fig. 4 we show that the mean relative error incurred by using the approximation  $\tilde{e}_4$  is smaller than 1% . However, the 95% percentile reaches a relative error of 3.5% inside the O<sub>2</sub>-A band. We equally show the effect of neglecting bandwise shifts by comparing emulations of  $e_4^\Lambda$  with  $e_4$  emulations with scalar shifts. The same parameters  $\tilde{\mathbf{p}}$  were used for  $e_4^\Lambda$  and  $e_4$  with only  $\Delta\lambda$  and  $\Delta\sigma$  set to a fixed scalar value for  $e_4$ . The relative errors can reach up to 10-20 % in the O<sub>2</sub>-A band highlighting the importance of bandwise sensor characterization.

#### 4.2. Reconstruction Performance

We evaluate the impact of the various implemented constraints, the optimization and the emulator extension on the reconstruction performance. To this end we compare the reconstruction performance of four different EmSFMNN set-ups to the reconstruction performance of an unconstrained least-squares optimization (LSQ) of the emulator  $e_4$  to individual pixels in a single HyPlant acquisition (cf. Fig. 5). By  $m_{\text{CKA}}(\tilde{e}_4)$  we denote an EmSFMNN predictor using the spectrally explicit sensor miscalibration emulator  $\tilde{e}_4$  and finetuned on the CKA-2020 (600 m) data set. The EmSFMNN  $m_{\text{SEL}}(\tilde{e}_4)$  and  $m_{\text{SEL}}(e_4)$  are equivalently trained on the SEL-2018 (600 m) data set and  $m_{\text{PRE}}(\tilde{e}_4)$  denotes the common backbone without finetuning. Importantly, the HyPlant acquisition for which we evaluate the reconstruction performance is part of the finetuning training set of  $m_{\text{SEL}}(\tilde{e}_4)$  but not of  $m_{\text{CKA}}(\tilde{e}_4)$ . Due to the prediction of  $\Delta\lambda$  and  $\Delta\sigma$  in EmSFMNN being dependent on learnable IDs, and the ID not having been trained for  $m_{\text{CKA}}(\tilde{e}_4)$ , we use a single ID in CKA that we arbitrarily choose from the set of IDs trained for CKA acquisitions.

	$e_4$	$e_4^\Lambda$	$\tilde{e}_4$
Prediction time per sample	0.28 $\mu\text{s}$	55.40 $\mu\text{s}$	1.93 $\mu\text{s}$

Table 4: Prediction time measurements for the original emulator  $e_4$ , the original emulator applied in a bandwise fashion  $e_4^\Lambda$  and the emulator approximation  $\tilde{e}_4$ . In the case of  $e_4$  only scalar sensor shifts were computed. The values represent the average of 20 time measurements on a single GPU (NVIDIA Quadro RTX 8000) predicting a batch of  $10^4$  samples.

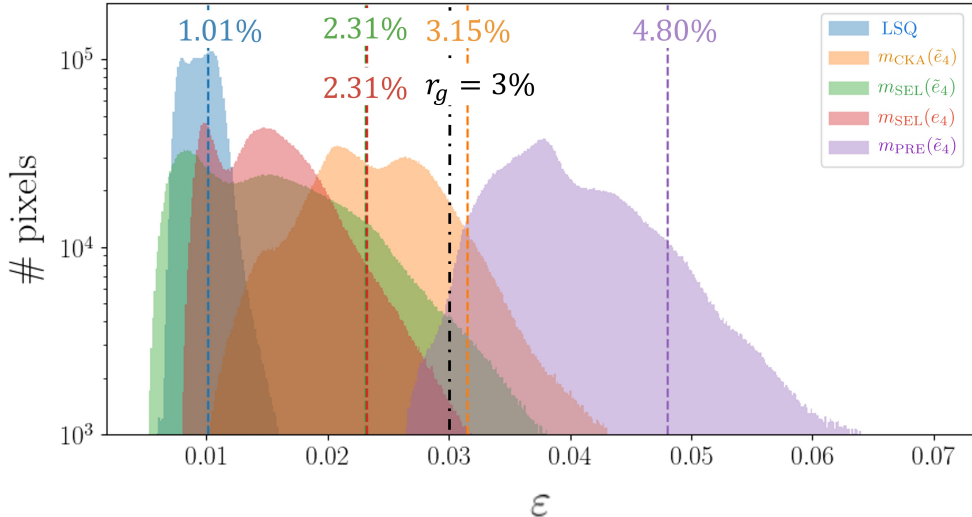


Figure 5: Distribution of relative reconstruction errors  $\varepsilon$  (see Eq. 13) for different EmSFMNN set-ups as well as a least-squares optimization in a HyPlant acquisition recorded on 2018/07/26 15:30 CEST in Selhausen. The mean values of these distributions are reported directly in the figure with vertical lines. Mean relative reconstruction errors for  $m_{\text{SEL}}(e_4)$  and  $m_{\text{SEL}}(\tilde{e}_4)$  overlap in this figure.  $r_g$  denotes the relative uncertainty of the radiometric calibration.

In Fig. 5 we report the distribution of the relative reconstruction residuals

$$\varepsilon = \left\langle \left| \frac{L_{\text{HyP}} - \hat{L}_{\text{HyP}}}{L_{\text{HyP}}} \right| \right\rangle_{x,\lambda}. \quad (13)$$

of LSQ and all EmSFMNN predictors in the acquisition. We find that the unconstrained emulator optimization LSQ outperforms all EmSFMNN training set-ups. However, since LSQ is completely unconstrained, the resulting estimates of physical parameters defining the simulation layer are not well disentangled. As a consequence, it cannot be used for SIF retrieval, even though it provides a useful baseline for the reconstruction error.

Since the simulation layer of  $m_{\text{SEL}}(e_4)$  and LSQ are the same, a comparison of  $m_{\text{SEL}}(e_4)$  to the least-squares optimization LSQ isolates the impact of EmSFMNN's constraint formulation and its feature-based optimization. The direct EmSFMNN equivalent  $m_{\text{SEL}}(e_4)$  performs significantly worse than LSQ, presumably due to the constrained optimization. However, this decrease in reconstruction performance can be improved by adopting the ex-

		<b>r</b>	<b>R<sup>2</sup></b>	<b>MAE</b> [mW nm <sup>-1</sup> sr <sup>-1</sup> m <sup>-2</sup> ]	<b>N</b>
SEL-2018 (600 m)	EmSFMNN ( $\tilde{e}_4$ )	0.91	0.55	<b>0.26 ± 0.09</b>	10
	EmSFMNN ( $e_4$ )	0.86	<b>0.74</b>	0.46 ± 0.05	10
	PRE	0.78	0.57	0.47 ± 0.06	10
	SFMNN	<b>0.98</b>	–	0.68 ± 0.07	10
	SFM	0.96	–	0.51 ± 0.07	10
	iFLD	0.64	0.10	0.88 ± 0.00	11
WST-2019 (1500 m)	EmSFMNN ( $\tilde{e}_4$ )	<b>-0.54</b>	–	<b>0.29 ± 0.05</b>	15
	EmSFMNN ( $e_4$ )	-0.73	–	1.48 ± 0.05	15
	PRE	-0.78	–	0.41 ± 0.04	15
	SFMNN	–	–	<b>0.22 ± 0.10</b>	15
	SFM	–	–	0.53 ± 0.08	15
	iFLD	–	–	0.80 ± 0.10	15
CKA-2020 (600 m)	EmSFMNN ( $\tilde{e}_4$ )	0.65	0.02	<b>0.35 ± 0.05</b>	16
	EmSFMNN ( $e_4$ )	0.69	0.18	0.47 ± 0.05	16
	PRE	0.67	–	0.39 ± 0.06	16
	SFMNN	0.69	<b>0.34</b>	<b>0.33 ± 0.06</b>	16
	SFM	<b>0.72</b>	–	0.48 ± 0.06	16
	iFLD	0.64	–	0.42 ± 0.09	16
CKA-2020 (350 m)	EmSFMNN ( $\tilde{e}_4$ )	0.74	0.04	<b>0.28 ± 0.04</b>	34
	EmSFMNN ( $e_4$ )	0.81	<b>0.12</b>	0.35 ± 0.04	34
	PRE	0.80	–	0.33 ± 0.04	34
	SFMNN	0.84	–	0.34 ± 0.04	34
	SFM	<b>0.87</b>	–	0.35 ± 0.04	34
	iFLD	0.58	0.05	<b>0.28 ± 0.05</b>	34
CKA-2021 (350 m)	EmSFMNN ( $\tilde{e}_4$ )	–	0.19	0.38 ± 0.09	6
	EmSFMNN ( $e_4$ )	–	0.16	1.07 ± 0.12	6
	PRE	–	0.30	0.70 ± 0.09	6
	SFMNN	–	–	0.65 ± 0.10	6
	SFM	–	–	0.50 ± 0.08	6
	iFLD	<b>0.85</b>	<b>0.71</b>	<b>0.12 ± 0.18</b>	6

Table 5: Comparative validation of SFM, iFLD, SFMNN and EmSFMNN retrieval methods. We report the mean absolute error (MAE) of the EmSFMNN predictions with respect to FLOX measurements, the Pearson correlation  $r$  and the Explained Variance Score  $R^2$ . In cases where the p-value of  $r$  is larger than 5% we do not report  $r$  and write – instead. Similarly, in cases where  $R^2 \leq 0$  we do not report  $R^2$  and write –.

tended emulator formulation with bandwise shift prediction which results in a smaller lower limit of the reconstruction residuals but which also increases the tail towards larger residuals.

We measure the generalization capacity of EmSFMNN across different data sets with respect to the reconstruction performance. The residual distribution of  $m_{\text{CKA}}(e_4)$  yields an  $\varepsilon$  which is significantly increased over its equivalent  $m_{\text{SEL}}(e_4)$  as it lacks finetuning to the HyPlant input data acquisition. However, its performance is close to what can be expected from the relative uncertainty of the radiometric calibration of the at-sensor radiance  $r_g$ . Since  $m_{\text{CKA}}(e_4)$  that has been finetuned on the CKA-2020 data set is applied here on an acquisition from the SEL-2018 data set, effects due to different yearly calibrations can affect the reconstruction performance.

Finally, it can be observed that the relative reconstruction error of  $m_{\text{PRE}}(e_4)$  is constrained in the range 3 - 6 %. It is thus larger than errors attributed purely to calibration uncertainties and indicates that the backbone PRE is not able to reconstruct model at-sensor radiance of arbitrary HyPlant acquisitions from its learned feature representation without prior finetuning.

#### 4.3. Validation with FLOX data

We validate EmSFMNN SIF predictions with top-of-canopy iFLD SIF estimates derived from radiance data recorded by FLOX devices. To this end, we use the fluorescence model assumption of the Gaussian implemented in the simulations to calculate  $\text{SIF}_{760}$  consistent with the FLOX iFLD retrieval software. Five measurement time series are at our disposal acquired during HyPlant overflights in field campaigns in the years 2018 - 2021 (see Fig. 6). To support our comparison, we also report the validation results for three baseline methods that were developed for hyperspectral HyPlant imagery (iFLD, SFM and SFMNN). Additionally, we show the impact of the emulator formulation and the finetuning on the performance of the standard training set-up denoted by EmSFMNN ( $\tilde{e}_4$ ) in Tab. 5. To this end, we report (i) results for the EmSFMNN set-up using the polynomial interpolation without band-wise sensor characterization, denoted as EmSFMNN ( $e_4$ ), and (ii) the performance of the coarsely pre-trained SIF predictor, denoted as PRE.

We find that the EmSFMNN ( $\tilde{e}_4$ ) predictors finetuned to the individual datasets generally are among the best SIF retrieval methods in terms of the mean absolute error with respect to FLOX estimates (MAE). They yield MAE scores consistently smaller than  $0.4 \text{ mW nm}^{-1} \text{ sr}^{-1} \text{ m}^{-2}$  whereas stronger variation in MAE can be found in case of the iFLD, SFM and

SFMNN SIF predictions. We find notably a reduced overestimating bias of EmSFMNN as compared to SFMNN in Fig. 6 and a higher accuracy than in SFM and iFLD predictions.

Both the use of  $\tilde{e}_4$  instead of  $e_4$  as well as the finetuning considerably decrease the MAE. This can be concluded from the improved performance of EmSFMNN ( $\tilde{e}_4$ ) over EmSFMNN ( $e_4$ ) and PRE. These two aspects have been introduced to improve

the model representation by (i) a more exact simulation layer in the reconstruction loss and (ii) a more precise fitting of the spectral data by specializing the network weights to a selection of HyPlant lines. While the use of the non-specialized pretrained EmSFMNN model PRE leads to validation results comparable to the baseline methods, it is necessary to make use of a finetuning step to improve over the baseline methods iFLD, SFM and SFMNN.

In Tab. 5 we equally report the Pearson correlation scores  $r$  and the Explained Variance Score  $R^2$ . A consistent cross-validation assessment based on  $r$  and  $R^2$  is, however, not possible throughout all validation data sets due to strongly variable performance under these two metrics. Due to the small number of validation data points these performance metrics are subject to large uncertainties. A reduced performance of EmSFMNN ( $\tilde{e}_4$ ) in terms of  $r$  with respect to SFMNN is, however, observable in all data sets where such a comparison can be made. We hypothesize that this may be due to the more strict modelling approach of EmSFMNN which may result in a higher sensitivity to sensor noise.

#### 4.4. Topography

The emulator was derived from simulations covering a  $h_{\text{gnd}}$  range of 0 - 0.76 km and of  $h_{\text{agl}}$  0.2 - 2.86 km. This allows the application of EmSFMNN predictors in acquisitions with large height variation where both the surface height  $h_{\text{gnd}}$  and flight height above ground level  $h_{\text{agl}}$  change significantly over the course of a single datatake. To test the reconstruction performance of EmSFMNN predictors under these circumstances we examine the TOPO data set consisting of HyPlant acquisitions with strong topographic variation and a nominal flight height of 600 m (see Tab. 1). We apply (i) the EmSFMNN predictor finetuned to the CKA-2020 (600 m) data set (denoted as  $m_{\text{CKA}}$ ) and (ii) a EmSFMNN finetuned to the TOPO data set ( $m_{\text{TOPO}}$ ). The finetuning of the  $m_{\text{TOPO}}$  and  $m_{\text{CKA}}$  was performed on the TOPO data set as described above (cf. Tab. 1) and only differed in the finetuning data

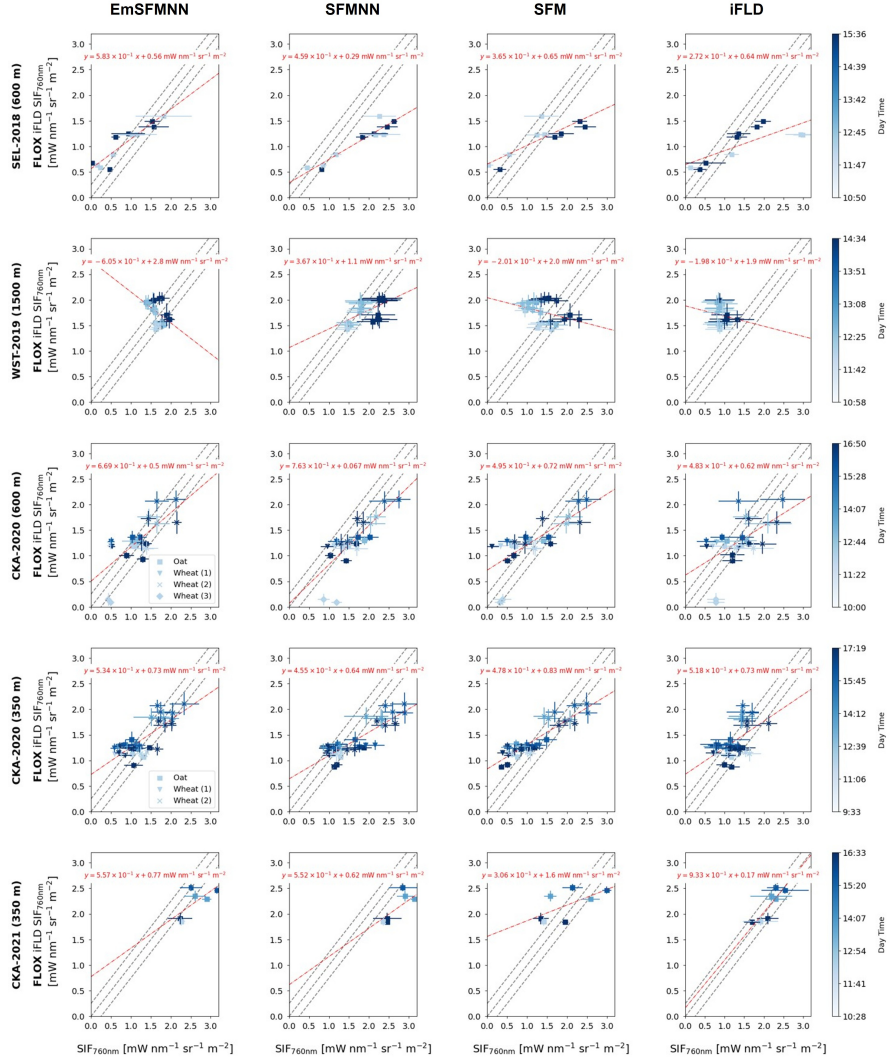


Figure 6: FLOX derived iFLD SIF vs. HyPlant derived EmSFMNN, SFMNN, SFM and iFLD SIF in the five in-situ validation data sets (see Tab. 1). The dashed line and the red floating labels report the linear relationship between EmSFMNN and FLOX iFLD estimates. In the CKA-2020 data sets FLOX measurements from different devices are reported separately.

set. Both predictors derive from a EmSFMNN backbone trained on the PRE data set which includes the data contained in TOPO. By examining

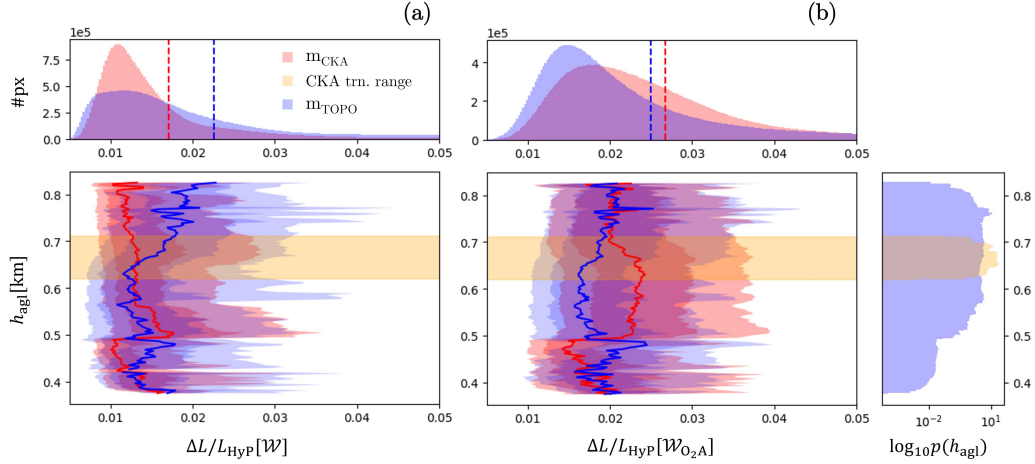


Figure 7: Top row: Marginalized distribution of relative reconstruction residuals of CKA(1) in red and TOPO(1) in blue in the whole fitted spectral window  $\mathcal{W}$  (a) and in the spectral window  $\mathcal{W}_{\text{O}_2\text{A}}$  in the O<sub>2</sub>-A band (b). Bottom left: Relative reconstruction residuals of CKA(1) (red) and TOPO(1) (blue) stratified by the sensor height above ground  $h_{\text{agl}}$  in  $\mathcal{W}$  (a) and  $\mathcal{W}_{\text{O}_2\text{A}}$  (b). Red and blue lines denote the means, dark areas denote the 25 - 75 percentile ranges, light areas denote the 10 - 90 percentile ranges. In yellow we highlight the range of  $h_{\text{agl}}$  covered by the CKA-2020 data set on which CKA(1) was finetuned. Bottom right: Logarithmic empirical histogram of  $h_{\text{agl}}$  of CKA-2020 in yellow and TOPO in blue.

on TOPO with both  $m_{\text{CKA}}$  and  $m_{\text{TOPO}}$  we can evaluate the importance of topography related distribution differences between finetuning data sets.

In Fig. 7 (a) and (b) we summarize the residual statistics of  $m_{\text{CKA}}$  and  $m_{\text{TOPO}}$  as a function of the flight height  $h_{\text{agl}}$  in the full prediction spectral window  $\mathcal{W}$  (750 - 770 nm) as well as in a narrow spectral window  $\mathcal{W}_{\text{O}_2\text{A}}$  in the O<sub>2</sub>-A absorption band (759.5 - 761 nm).  $m_{\text{CKA}}$  outperforms the finetuned  $m_{\text{TOPO}}$  in  $\mathcal{W}$  exhibiting a residual distribution with less outliers. Notably,  $m_{\text{CKA}}$  outperforms  $m_{\text{TOPO}}$  including in  $h_{\text{agl}}$  ranges that are not covered by the CKA-2020 (600 m) finetuning data set. The finetuning to the validation data set TOPO yields, however, to an improved  $m_{\text{TOPO}}$  performance in the O<sub>2</sub>-A band with  $m_{\text{TOPO}}$  exhibiting an improved reconstruction performance overall. The strong reconstruction residual outliers of  $m_{\text{TOPO}}$  are consequently contained in spectral regions outside the O<sub>2</sub>-A band as can be understood from the fact that its performance on  $\mathcal{W}_{\text{O}_2\text{A}}$  is less affected by it.

While we are able to assess the reconstruction performance of  $m_{\text{TOPO}}$  and  $m_{\text{CKA}}$ , we can not evaluate the SIF predictions in the TOPO data set

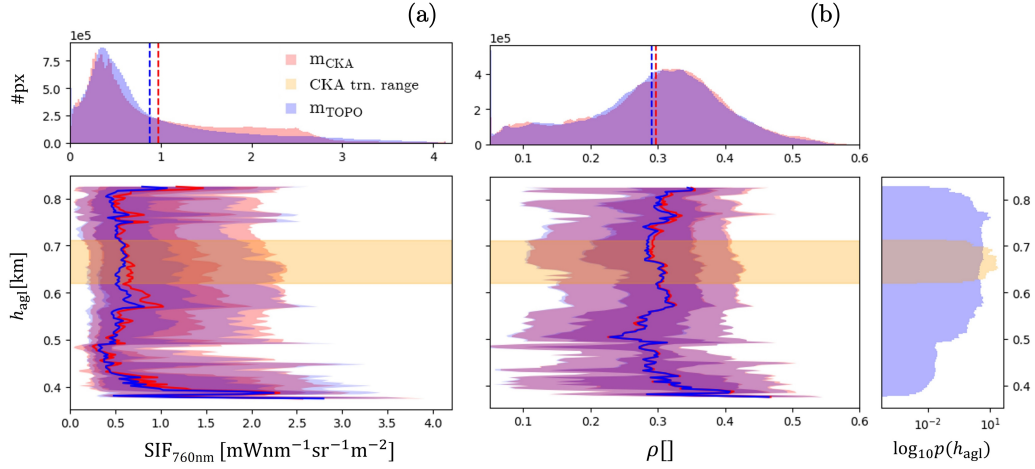


Figure 8: Top row: Marginalized distribution of reflectance offset parameter  $\rho$  (a) and fluorescence emission amplitude  $F_{737}$  as predicted by CKA(1) in red and TOPO(1) in blue. Bottom left: reflectance offset parameter  $\rho$  (a) and fluorescence emission amplitude  $F_{737}$  (b) stratified by the sensor height above ground  $h_{\text{agl}}$  as predicted by CKA(1) in red and by TOPO(1) in blue. Red and blue lines denote the means, dark areas denote the 25 - 75 percentile ranges, light areas denote the 10 - 90 percentile ranges. In yellow we highlight the range of  $h_{\text{agl}}$  covered by the CKA-2020 data set on which CKA(1) was finetuned. Bottom right: Logarithmic empirical histogram of  $h_{\text{agl}}$  of CKA-2020 in yellow and TOPO in blue.

due to lacking in-situ data. Therefore, we test whether in addition to the reconstruction performance the SIF prediction and reflectance estimation are independent of the  $h_{\text{agl}}$  variation. Fig. 8 (a) shows that the SIF predictions of  $m_{\text{TOPO}}$  and  $m_{\text{CKA}}$  have a constant mean over most of the covered height range. This is to be expected in the case of a homogeneous distribution of fluorescence emitting surfaces. The decoupling of  $h_{\text{agl}}$  from the SIF prediction is only invalid in the range  $h_{\text{agl}} < 0.5$  km where both  $m_{\text{TOPO}}$  and  $m_{\text{CKA}}$  have a larger mean SIF prediction than in the rest of the height range. There are however significantly less HyPlant pixels falling in this range such that the homogeneity assumption is weakened due to a decreased statistical relevance.

In Fig. 9 we show an exemplary HyPlant acquisition that highlights the independence of the achieved SIF prediction and the reconstruction performance from  $h_{\text{agl}}$ . Both SIF and the fractional residual  $\Delta L/L_{\text{HyP}}$  are unaffected by the topographic variation over the hill slope in the image center. The SIF predictions differ only slightly in  $m_{\text{TOPO}}$  and  $m_{\text{CKA}}$  due to differences in the finetuning training data set.

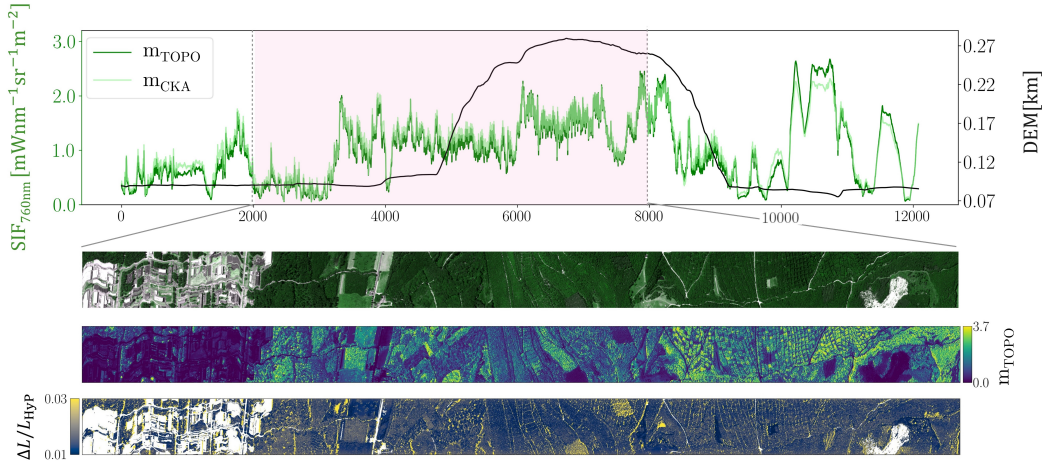


Figure 9: Top row: Shown are the SIF prediction of TOPO(1) and CKA(1) along the ground surface altitude  $h_{\text{gnd}}$  derived from a matching Digital Elevation Map (DEM). Lower rows: shown are a false color image of the HyPlant at-sensor radiance, the pixelwise SIF prediction of TOPO and the relative reconstruction error of TOPO in the spectral window  $\mathcal{W}$  in a subset of the HyPlant acquisition displayed in the top row.

Concluding, we can observe that the influence  $h_{\text{agl}}$  on EmSFMNN’s reconstruction performance, SIF and reflectance prediction is small. The variation of reconstruction errors, SIF and reflectance of both  $m_{\text{TOPO}}$  and  $m_{\text{CKA}}$  do not vary systematically with  $h_{\text{agl}}$ . It could be observed that the choice of the training data set for finetuning had a larger effect on EmSFMNN’s reconstruction performance than the topographic variation indicating that EmSFMNN can compensate for the variability in the atmospheric transfer with the specific choice of RTM emulation adopted in this contribution.

## 5. Discussion

### 5.1. Simulation and Emulator Design and Limitations

In this work the integrated use of a polynomial emulator and self-supervised neural network training could be shown to yield both fast and accurate estimation of SIF at 760 nm. Two design choices of the simulation model are of particular relevance to the discussion of EmSFMNN’s performance.

Firstly, the model underlying the simulation tool and the emulator was set up to not feature any cross-correlation between input parameters. Making use of a physiologically plausible model such as SCOPE [7] relation-

ships would have confounded EmSFMNN’s capacity to fit the at-sensor radiance signal purely on the basis of physical principles with possible cross-correlations between estimated parameters. As an example, it is well known that both the reflectance in the spectral region of photosynthetically active radiation (PAR) and the total fluorescence emission amplitude  $F_{737}$  are strongly correlated in green vegetation due to a common dependency on leaf chlorophyll concentration [40]. Reconstructed SIF products involving space-borne reflectance products such as the MODIS-based RSIF [41] and RTSIF [42], reconstructing the TROPOMI SIF product, make use of this relationship. Detailed studies with field data could also establish cross-correlations in reflectance-based features and top-of-canopy SIF derived from airborne platforms resulting from structural effects [43, 44] and biochemical processes related to non-photochemical quenching [45]. However, such dependencies, if incorporated a-priori in the predictor modelling assumptions, may well induce larger gradients in the self-supervised loss than the small at-sensor fluorescence signal. As a consequence, the influence of such correlations on the feature-based optimization and ultimately on the SIF estimate may trump the physical and causal relationship leveraged in EmSFMNN.

Secondly, this contribution has focused on SIF retrieval in a narrow spectral range. The spectral range around the O<sub>2</sub>-A absorption band of the simulation data base has allowed us to (1) parametrize the reflectance and fluorescence with simple functions (second-order polynomial, Gaussian) and (2) use a polynomial model to approximate the simulation data base. The polynomial form chosen for the emulator was advantageous to the EmSFMNN set-up as it allowed an easy integration of the emulator in the neural network architecture: both forward pass and backward gradient computation were achieved by implementing the emulator as a fixed linear layer.

The use of the plain polynomial emulator  $e_4$  [28, 27] for EmSFMNN has led to subpar performance with respect to in-situ FLOX measurements. While the lacking spectrally explicit sensor characterization did not lead necessarily to decreased performance in terms of spectral reconstruction residuals, the emulator model’s incompleteness has caused systematic errors in the signal decomposition. As a consequence, we have implemented an emulator capable of simulating HyPlant at-sensor radiances with bandwise spectral shifts with an efficient approximation  $\tilde{e}_4$ . This approximation could be shown to yield acceptable relative errors peaking at  $\sim 3.5\%$  with respect to the exact, but computationally demanding emulator solution  $e_4^\Lambda$ . The error

incurred by the approximation in the O<sub>2</sub>-A absorption band may, however, still be significant in terms of reconstruction accuracy considering that the mean fluorescence emission at 760 nm in HyPlant acquisition amounts also to < 3% of the mean at-sensor signal. The validation of the SIF prediction of EmSFMNN models integrating this approximate emulator  $\tilde{e}_4$  proved sufficient to outperform all baseline methods in terms of accuracy.

While we have shown the application of EmSFMNN to HyPlant FLUO data in this contribution, the EmSFMNN approach to retrieve SIF can be implemented for data from different imaging sensors (e.g., [25]) and spectral regions. Since the network architecture interacts with the data in the loss only through the interface of the emulator representing the physical constraints of the retrieval problem, such a change in the data modality would simply necessitate adapting the emulator. In particular, the modelling of the sensor in the simulation tool [11] and an extension of the reflectance and fluorescence parametric functions to the new spectral range would be required. Further research in emulator representations of simulated hyperspectral at-sensor radiance including bandwise sensor characterization is thus warranted. While the simple polynomial approach adopted here was suitable for the spectral range and simulation model that had been fixed for the EmSFMNN O<sub>2</sub>-A SIF retrieval problem on HyPlant data, the integration of different emulator architectures [46, 47, 48] may become necessary for retrieval in different data modalities.

### 5.2. Prediction of Atmospheric Variables

We have tested the quality of EmSFMNN's signal decomposition with respect to its reconstruction performance and the agreement of its SIF prediction with in-situ measurements. We could not validate the accuracy of the predicted atmospheric variables (water vapour content H<sub>2</sub>O and aerosol optical thickness AOT<sub>550</sub>) with direct measurements. The prediction of these variables is understood to be very challenging in the setting adopted in the presented retrieval method since (i) the sensitivity of the at-sensor radiance to water vapour and AOT<sub>550</sub> in the fitting spectral window (750 - 770 nm) is small [11], (ii) the variation of both parameters in the training data is expected to be small due to similar meteorological conditions during HyPlant campaigns. Furthermore, there may be remaining representation insufficiencies of the emulator  $e_4$  that can result in EmSFMNN predictors leveraging the degrees of freedom in these parameters to adjust the atmospheric estimate

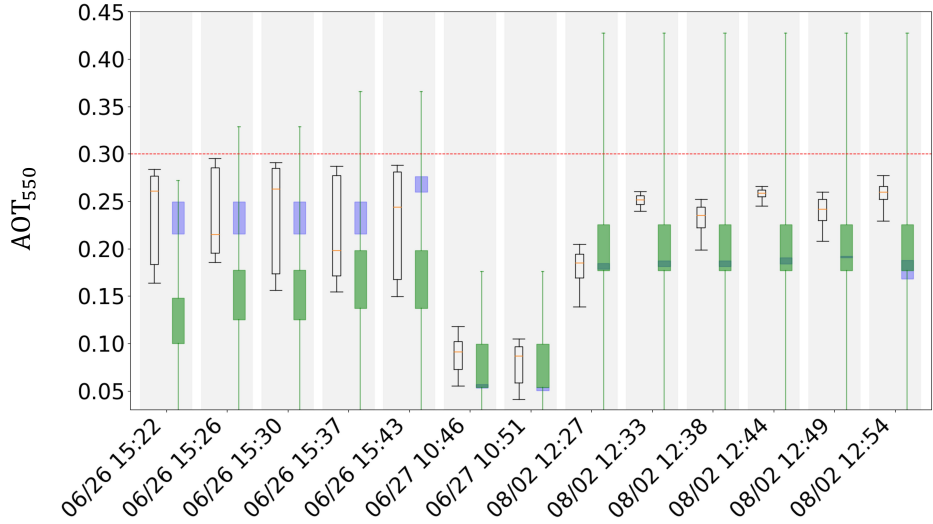


Figure 10: Comparison of  $AOT_{550}$  estimates. *Black*: distribution of EmSFMNN  $AOT_{550}$  estimates in single HyPlant acquisitions, box width show 25-75 % percentiles and whiskers show 5 -95% percentiles, the median is reported in orange, *Blue*: CIMEL measurements of the JOYCE AERONET station [49] located at  $\sim 5$  km from the SEL-2018 HyPlant acquisitions (left), box width shows the standard deviation of all measurements recorded within 20 minutes of the HyPlant acquisition time, *Green*: Deep Blue  $AOT_{550}$  products of MODIS Terra [50] and Aqua [51] at 10 km resolution, box width shows the standard deviation of available Terra and Aqua products within two hours of the HyPlant acquisition time and the whiskers represent the mean of the provided uncertainty of the estimates within a 30 km window around the location of the CKA-2020 estimates. *Red*: maximum  $AOT_{550}$  covered in simulation data base.

to the observational data. In particular, we highlight that the at-sensor radiance simulations all have used a standardized atmospheric pressure profile (MODTRAN *mid-latitude summer*) while we have not adapted the emulator to the meteorological conditions at acquisition time. Thus, while  $H_2O$  and  $AOT_{550}$  were included explicitly in the simulations and EmSFMNN addresses these parameters with a spatial constraint, accurate retrieval of these parameters can not be expected.

We show in Fig. 10, however, that the distributions of  $AOT_{550}$  estimates of single HyPlant acquisitions is approximately consistent with  $AOT_{550}$  measurements of a CIMEL instrument located in the JOYCE AERONET station [49] nearby the geographical center of HyPlant acquisitions in the SEL-2018 data set ( $\sim 5$  km). We could gather for this analysis CIMEL  $AOT_{550}$  measurements with a maximum time difference to the HyPlant acquisition

time of 20 minutes. In particular, we find a strong decrease in  $\text{AOT}_{550}$  on 2018/06/27 which is reflected in EmSFMNN estimates as well. Furthermore, MODIS Terra and Aqua  $\text{AOT}_{550}$  estimates from data with a maximum two hour time difference to the HyPlant acquisition are similar to EmSFMNN. The MODIS estimates exhibit large uncertainties, however, such that they must be considered to gauge only very roughly the accuracy of EmSFMNN  $\text{AOT}_{550}$ .

A more detailed study of parameters pertaining to the atmospheric composition at acquisition time would be of relevance for EmSFMNN if it were to be applied to more susceptible spectral regions covered by full-spectrum retrieval. Furthermore, more extensive analysis could establish the performance benefit of including atmospheric estimates from different sensors as in [25]. Since such a procedure is planned with the FLEX/Sentinel-3 tandem orbit configuration [22], such analysis is relevant especially for further work on the application of EmSFMNN on FLEX data.

### 5.3. Feature Generalization of EmSFMNN

The validation analyses have shown good performance of EmSFMNN models on data for which the models were not finetuned. In Section 4.2 we could show that  $m_{\text{CKA}}(\tilde{e}_4)$  applied to a HyPlant acquisition from SEL-2018 yielded a mean reconstruction performance of  $\epsilon < 3.15\%$  as compared to the result of the finetuned  $m_{\text{SEL}}(\tilde{e}_4)$  of  $\epsilon < 2.31\%$ . In addition to the reconstruction performance being similar, Section 4.3 could establish that the non-finetuned backbone predictor PRE could estimate SIF outperforming the SFM, iFLD and SFMNN baselines in some of the validation data sets. The SEL-2018 data set is similar to CKA-2020 on which  $m_{\text{CKA}}(\tilde{e}_4)$  was finetuned. Its  $h_{\text{agl}}$  and  $h_{\text{gnd}}$  ranges are overlapping. Furthermore, both data sets cover predominantly agricultural fields and exhibit only a small fraction of forested areas such that  $m_{\text{CKA}}(\tilde{e}_4)$  and  $m_{\text{SEL}}(\tilde{e}_4)$  are trained with a similar spectral surface composition. However, the data sets were acquired in different years resulting in varying radiometric sensor calibrations associated with a mean uncertainty of 3%. These results indicate that EmSFMNN generalizes well across HyPlant data sets with large similarities.

Furthermore, a generalization capability of EmSFMNN across topographic changes could be established in Section 4.4. We could show that  $m_{\text{CKA}}(\tilde{e}_4)$ , which was finetuned on data exhibiting only small topographic variation, had an improved reconstruction performance over an EmSFMNN instance that was finetuned on the full topographic range present in TOPO. We interpret

this finding such that the learned feature space successfully disentangles features that are unrelated to the topographic change and the associated optical path length differences (i.e. the reflectance and SIF emission). This in turn is corroborated by the observation that both the statistical distribution of the predicted SIF emission as well as of the reflectance are constant across the full topographic range.

The possibility to base the inference of SIF in new data on a single generalized SIF retrieval model is an advantage of the feature based optimization of EmSFMNN over other physical SIF retrieval methods for which a repeated pixelwise or campaign-wise optimization has to be conducted. While we have not conducted validation studies on completely new data sources, that were not included in the pretraining or finetuning training data, we could show that the EmSFMNN could be finetuned successfully to a range of HyPlant data sets without complete retraining. If the importance of finetuning on the SIF prediction performance could be better quantified and reduced, the emulator based SIF retrieval method developed here could therefore prove to be a useful contribution to efficient SIF retrieval method for hyperspectral high-throughput imaging sensors where inference speed is critical.

## 6. Conclusion

In this work, we have applied EmSFMNN, a novel emulation-based SIF retrieval method first presented by [25], to HyPlant FLUO acquisitions. EmSFMNN utilizes feature-based optimization and hyperspectral RTM emulation to disentangle the fluorescence signal from the at-sensor radiance. It has first been introduced in an application with DESIS data [25]. We have proposed an extension to the originally purely polynomial model used for DESIS to represent spectrally explicit CW and FWHM shifts computationally efficiently. This has allowed for the training of EmSFMNN on a significant fraction of the totality of available HyPlant acquisitions.

The direct SIF validation with in-situ SIF estimates derived from FLOX measurements has shown that the accuracy of finetuned EmSFMNN outperforms both SFMNN as well as traditional baseline methods (SFM, iFLD). Importantly, we could also show that a pretrained backbone EmSFMNN predictor generalized well across the considered HyPlant campaigns such that improved EmSFMNN SIF retrievals could be achieved at a smaller computational cost than traditional pixel-wise optimization. The computational

efficiency of this approach is due to the feature-based nature of EmSFMNN that allows a single model to be used for inference without prior finetuning.

Furthermore, in an analysis with HyPlant acquisition with strong topographic variability, we could show that the set-up allows for a generalization of the application domain of SIF retrieval. The possibility to constrain the retrieval by exact topography and geometrical information has allowed the application of EmSFMNN to HyPlant acquisitions with strong topographic variation where prior retrieval algorithms could not be applied in a straightforward fashion.

Finally, we have presented a small comparison of EmSFMNN predicted  $AOT_{550}$  with high-fidelity CIMEL  $AOT_{550}$  measurements in a single campaign data set consisting of 13 acquisitions giving first insights into the accuracy of the atmospheric characterization estimated by EmSFMNN. We found a consistent variation of predicted  $AOT_{550}$  with the measurements which supports the hypothesis that the disentangling of reflectance, fluorescence and atmospheric components as predicted by EmSFMNN is trustworthy. Further work is, however, necessary to assess EmSFMNN’s performance in predicting secondary atmospheric components in general observation conditions.

As HyPlant FLUO is the airborne demonstrator for the spaceborne FLORIS sensor, that will be operated onboard ESA’s Earth Explorer mission, this work is relevant for further research in computationally efficient SIF retrieval algorithms for data acquired by FLORIS. While [25] have shown how EmSFMNN could be applied to radiance data acquired on a spaceborne platform, in this work we have focused specifically on the requirements of HyPlant FLUO, a sensor comparable to FLORIS. The encouraging results in terms of precision in both DESIS and HyPlant FLUO suggest that EmSFMNN may be successfully applied to FLORIS data as well.

## 7. Acknowledgements

This work is part of the project “FluoMap” (Impulsfonds-Förderkennzeichen ZT-I-PF-5-12) funded by the Helmholtz Initiative and Networking Fund, Helmholtz AI, Deutsches Zentrum für Luft- und Raumfahrt (DLR) and Forschungszentrum Jülich GmbH (FZJ). The authors gratefully acknowledge computing time on the supercomputer JURECA [52] at Forschungszentrum Jülich under grant no. fluomap-ct. We gratefully acknowledge the financial support by the European Space Agency (ESA) for airborne data acquisition and data analysis in the frame of the FLEXSense campaign (ESA

Contract No. 4000125402/ 18/NL/NA) and the Photoproxy project (ESA contract No. 4000125731/19/NL/LF). Additionally, HyPlant and FLOX data acquisition have partially been funded by the German Federal Ministry of Education and Research within the German-Plant-Phenotyping Network (DPPN) (project identification number: 031A053), the ‘Strukturwandel-Projekt Bioökonomie REVIER’, which is funded by the German Federal Ministry of Education and Research (project identification number 031B0918A), the Deutsche Forschungsgemeinschaft (DFG, German Research Foundation) under Germany’s Excellence Strategy – EXC 2070–390732324 and the project Land surface Interactions with the Atmosphere over the Iberian Semi-arid Environment (LIAISE) funded by the Centre national de la recherche scientifique (CNRS). Open access is funded by the Deutsche Forschungsgemeinschaft (DFG, German Research Foundation) – 491111487.

## References

- [1] A. Berk, P. Conforti, R. Kennett, T. Perkins, F. Hawes, J. van den Bosch, MODTRAN® 6: A major upgrade of the MODTRAN® radiative transfer code, in: 2014 6th Workshop on Hyperspectral Image and Signal Processing: Evolution in Remote Sensing (WHISPERS), 2014, pp. 1–4. [doi:10.1109/WHISPERS.2014.8077573](https://doi.org/10.1109/WHISPERS.2014.8077573).
- [2] S. Y. Kotchenova, E. F. Vermote, R. Matarrese, Jr. Frank J. Klemm, Validation of a vector version of the 6S radiative transfer code for atmospheric correction of satellite data. Part I: Path radiance, *Applied Optics* 45 (26) (2006) 6762–6774. [doi:10.1364/AO.45.006762](https://doi.org/10.1364/AO.45.006762).
- [3] S. Y. Kotchenova, E. F. Vermote, Validation of a vector version of the 6S radiative transfer code for atmospheric correction of satellite data. Part II. Homogeneous Lambertian and anisotropic surfaces, *Applied Optics* 46 (20) (2007) 4455–4464. [doi:10.1364/AO.46.004455](https://doi.org/10.1364/AO.46.004455).
- [4] C. Emde, R. Buras-Schnell, A. Kylling, B. Mayer, J. Gasteiger, U. Hamann, J. Kylling, B. Richter, C. Pause, T. Dowling, L. Bugliaro, The libRadtran software package for radiative transfer calculations (version 2.0.1), *Geoscientific Model Development* 9 (5) (2016) 1647–1672. [doi:10.5194/gmd-9-1647-2016](https://doi.org/10.5194/gmd-9-1647-2016).
- [5] S. Jacquemoud, F. Baret, PROSPECT: A model of leaf optical properties spectra, *Remote Sensing of Environment* 34 (2) (1990) 75–91. [doi:10.1016/0034-4257\(90\)90100-Z](https://doi.org/10.1016/0034-4257(90)90100-Z).
- [6] J.-B. Feret, C. François, G. P. Asner, A. A. Gitelson, R. E. Martin, L. P. Bidel, S. L. Ustin, G. Le Maire, S. Jacquemoud, PROSPECT-4 and 5: Advances in the leaf optical properties model separating photosynthetic pigments, *Remote Sensing of Environment* 112 (6) (2008) 3030–3043. [doi:10.1016/j.rse.2008.02.012](https://doi.org/10.1016/j.rse.2008.02.012).
- [7] C. Van Der Tol, W. Verhoef, J. Timmermans, A. Verhoef, Z. Su, An integrated model of soil-canopy spectral radiances, photosynthesis, fluorescence, temperature and energy balance, *Biogeosciences* 6 (12) (2009) 3109–3129. [doi:10.5194/bg-6-3109-2009](https://doi.org/10.5194/bg-6-3109-2009).

- [8] C. Van Der Tol, W. Verhoef, A. Rosema, A model for chlorophyll fluorescence and photosynthesis at leaf scale, *Agricultural and Forest Meteorology* 149 (1) (2009) 96–105. [doi:10.1016/j.agrformet.2008.07.007](https://doi.org/10.1016/j.agrformet.2008.07.007).
- [9] S. Jacquemoud, W. Verhoef, F. Baret, C. Bacour, P. J. Zarco-Tejada, G. P. Asner, C. François, S. L. Ustin, PROSPECT+SAIL models: A review of use for vegetation characterization, *Remote Sensing of Environment* 113 (2009) S56–S66. [doi:10.1016/j.rse.2008.01.026](https://doi.org/10.1016/j.rse.2008.01.026).
- [10] J.-P. Gastellu-Etchegorry, T. Yin, N. Lauret, T. Cajgfinger, T. Gregoire, E. Grau, J.-B. Feret, M. Lopes, J. Guilleux, G. Dedieu, Z. Malenovský, B. Cook, D. Morton, J. Rubio, S. Durrieu, G. Cazanave, E. Martin, T. Ristorcelli, Discrete Anisotropic Radiative Transfer (DART 5) for Modeling Airborne and Satellite Spectroradiometer and LIDAR Acquisitions of Natural and Urban Landscapes, *Remote Sensing* 7 (2) (2015) 1667–1701. [doi:10.3390/rs70201667](https://doi.org/10.3390/rs70201667).
- [11] M. Pato, K. Alonso, J. Buffat, S. Auer, E. Carmona, S. Maier, R. Müller, P. Rademske, U. Rascher, H. Scharr, Simulation Framework for Solar-Induced Fluorescence Retrieval and Application to Desis and Hyplant (Feb. 2025). [doi:10.2139/ssrn.5148562](https://doi.org/10.2139/ssrn.5148562).
- [12] F. Daumard, Y. Goulas, A. Ounis, R. Pedrós, I. Moya, Measurement and Correction of Atmospheric Effects at Different Altitudes for Remote Sensing of Sun-Induced Fluorescence in Oxygen Absorption Bands, *IEEE Transactions on Geoscience and Remote Sensing* 53 (9) (2015) 5180–5196. [doi:10.1109/TGRS.2015.2418992](https://doi.org/10.1109/TGRS.2015.2418992).
- [13] S. Cogliati, W. Verhoef, S. Kraft, N. Sabater, L. Alonso, J. Vicent, J. Moreno, M. Drusch, R. Colombo, Retrieval of sun-induced fluorescence using advanced spectral fitting methods, *Remote Sensing of Environment* 169 (2015) 344–357. [doi:10.1016/j.rse.2015.08.022](https://doi.org/10.1016/j.rse.2015.08.022).
- [14] N. Sabater, J. Vicent, L. Alonso, J. Verrelst, E. M. Middleton, A. Porcar-Castell, J. Moreno, Compensation of Oxygen Transmittance Effects for Proximal Sensing Retrieval of Canopy-Leaving Sun-Induced Chlorophyll Fluorescence, *Remote Sensing* 10 (10) (2018) 1551. [doi:10.3390/rs10101551](https://doi.org/10.3390/rs10101551).

- [15] S. Cogliati, M. Celesti, I. Cesana, F. Miglietta, L. Genesio, T. Julitta, D. Schuettemeyer, M. Drusch, U. Rascher, P. Jurado, R. Colombo, A Spectral Fitting Algorithm to Retrieve the Fluorescence Spectrum from Canopy Radiance, *Remote Sensing* 11 (16) (2019) 1840. [doi:10.3390/rs11161840](https://doi.org/10.3390/rs11161840).
- [16] S. Wieneke, H. Ahrends, A. Damm, F. Pinto, A. Stadler, M. Rossini, U. Rascher, Airborne based spectroscopy of red and far-red sun-induced chlorophyll fluorescence: Implications for improved estimates of gross primary productivity, *Remote Sensing of Environment* 184 (2016) 654–667. [doi:10.1016/j.rse.2016.07.025](https://doi.org/10.1016/j.rse.2016.07.025).
- [17] W. Verhoef, H. Bach, Simulation of hyperspectral and directional radiance images using coupled biophysical and atmospheric radiative transfer models, *Remote Sensing of Environment* 87 (1) (2003) 23–41. [doi:10.1016/S0034-4257\(03\)00143-3](https://doi.org/10.1016/S0034-4257(03)00143-3).
- [18] L. Guanter, L. Alonso, L. Gómez-Chova, M. Meroni, R. Preusker, J. Fischer, J. Moreno, Developments for vegetation fluorescence retrieval from spaceborne high-resolution spectrometry in the O2-A and O2-B absorption bands, *Journal of Geophysical Research: Atmospheres* 115 (D19) (2010). [doi:10.1029/2009JD013716](https://doi.org/10.1029/2009JD013716).
- [19] A. Damm, L. Guanter, V. C. E. Laurent, M. E. Schaepman, A. Schickling, U. Rascher, FLD-based retrieval of sun-induced chlorophyll fluorescence from medium spectral resolution airborne spectroscopy data, *Remote Sensing of Environment* 147 (2014) 256–266. [doi:10.1016/j.rse.2014.03.009](https://doi.org/10.1016/j.rse.2014.03.009).
- [20] T. L. Anderson, R. J. Charlson, D. M. Winker, J. A. Ogren, K. Holmén, Mesoscale Variations of Tropospheric Aerosols\*, *Journal of the Atmospheric Sciences* 60 (1) (2003) 119–136. [doi:10.1175/1520-0469\(2003\)060<0119:MVOTA>2.0.CO;2](https://doi.org/10.1175/1520-0469(2003)060<0119:MVOTA>2.0.CO;2).
- [21] D. R. Thompson, B. H. Kahn, P. G. Brodrick, M. D. Lebsack, M. Richardson, R. O. Green, Spectroscopic imaging of sub-kilometer spatial structure in lower-tropospheric water vapor, *Atmospheric Measurement Techniques* 14 (4) (2021) 2827–2840. [doi:10.5194/amt-14-2827-2021](https://doi.org/10.5194/amt-14-2827-2021).

[22] M. Drusch, J. Moreno, U. Del Bello, R. Franco, Y. Goulas, A. Huth, S. Kraft, E. M. Middleton, F. Miglietta, G. Mohammed, L. Nedbal, U. Rascher, D. Schüttemeyer, W. Verhoef, The FLuorescence EXplorer Mission Concept—ESA’s Earth Explorer 8, *IEEE Transactions on Geoscience and Remote Sensing* 55 (3) (2017) 1273–1284. [doi:10.1109/TGRS.2016.2621820](https://doi.org/10.1109/TGRS.2016.2621820).

[23] D. R. Thompson, N. Bohn, P. G. Brodrick, N. Carmon, M. L. Eastwood, R. Eckert, C. G. Fichot, J. P. Harringmeyer, H. M. Nguyen, M. Simard, A. K. Thorpe, Atmospheric Lengthscales for Global VSWIR Imaging Spectroscopy, *Journal of Geophysical Research: Biogeosciences* 127 (6) (2022) e2021JG006711. [doi:10.1029/2021JG006711](https://doi.org/10.1029/2021JG006711).

[24] J. Buffat, M. Pato, K. Alonso, S. Auer, E. Carmona, S. Maier, R. Müller, P. Rademske, B. Siegmann, U. Rascher, H. Scharr, A multi-layer perceptron approach for SIF retrieval in the O<sub>2</sub>-A absorption band from hyperspectral imagery of the HyPlant airborne sensor system, *Remote Sensing of Environment* 318 (2025) 114596. [doi:10.1016/j.rse.2024.114596](https://doi.org/10.1016/j.rse.2024.114596).

[25] J. Buffat, M. Pato, K. Alonso, S. Auer, E. Carmona, S. Maier, R. Müller, P. Rademske, U. Rascher, H. Scharr, Retrieval of sun-induced plant fluorescence in the O<sub>2</sub>-A absorption band from DESIS imagery, accepted for publication in the ECCV Workshop Proceedings at CVPPA 2024. (Nov. 2024). [arXiv:2411.08925](https://arxiv.org/abs/2411.08925), [doi:10.48550/arXiv.2411.08925](https://doi.org/10.48550/arXiv.2411.08925).

[26] J. Vicent Servera, J. P. Rivera-Caicedo, J. Verrelst, J. Muñoz-Marí, N. Sabater, B. Berthelot, G. Camps-Valls, J. Moreno, Systematic Assessment of MODTRAN Emulators for Atmospheric Correction, *IEEE Transactions on Geoscience and Remote Sensing* 60 (2022) 1–17. [doi:10.1109/TGRS.2021.3071376](https://doi.org/10.1109/TGRS.2021.3071376).

[27] M. Pato, J. Buffat, K. Alonso, S. Auer, E. Carmona, S. Maier, R. Müller, P. Rademske, U. Rascher, H. Scharr, Physics-based Machine Learning Emulator of At-sensor Radiances for Solar-induced Fluorescence Retrieval in the O<sub>2</sub>-A Absorption Band, *IEEE Journal of Selected Topics in Applied Earth Observations and Remote Sensing* (2024) 1–10 [doi:10.1109/JSTARS.2024.3457231](https://doi.org/10.1109/JSTARS.2024.3457231).

[28] M. Pato, K. Alonso, S. Auer, J. Buffat, E. Carmona, S. Maier, R. Müller, P. Rademske, U. Rascher, H. Scharr, Fast Machine Learning Simula-

tor of At-Sensor Radiances for Solar-Induced Fluorescence Retrieval with DESIS and Hyplant, in: IGARSS 2023 - 2023 IEEE International Geoscience and Remote Sensing Symposium, 2023, pp. 7563–7566. [doi:10.1109/IGARSS52108.2023.10281579](https://doi.org/10.1109/IGARSS52108.2023.10281579).

[29] B. Siegmann, L. Alonso, M. Celesti, S. Cogliati, R. Colombo, A. Damm, S. Douglas, L. Guanter, J. Hanuš, K. Kataja, T. Kraska, M. Matveeva, J. Moreno, O. Muller, M. Pikl, F. Pinto, J. Quirós Vargas, P. Rademske, F. Rodriguez-Moreno, N. Sabater, A. Schickling, D. Schüttemeyer, F. Zemek, U. Rascher, The High-Performance Airborne Imaging Spectrometer HyPlant—From Raw Images to Top-of-Canopy Reflectance and Fluorescence Products: Introduction of an Automatized Processing Chain, *Remote Sensing* 11 (23) (2019) 2760. [doi:10.3390/rs11232760](https://doi.org/10.3390/rs11232760).

[30] J. Buffat, U. Rascher, P. Rademske, B. Siegmann, L. V. Junker-Frohn, D. Emin, HyData: HyPlant FLUO at-sensor radiance data packages and FLOX measurements for SIF retrieval method development from selected campaigns of the years 2018 - 2023 (2024). [doi:10.26165/JUELICH-DATA/QKJKPW](https://doi.org/10.26165/JUELICH-DATA/QKJKPW).

[31] European Space Agency, Technical assistance for the deployment of an advanced hyperspectral imaging sensor during FLEX-EU (Sep. 2017). [doi:10.5270/ESA-20835d4](https://doi.org/10.5270/ESA-20835d4).

[32] European Space Agency, Technical Assistance for the Deployment of an advanced hyperspectral imaging sensor during SoyFLEX (Oct. 2017). [doi:10.5270/ESA-50a3dd4](https://doi.org/10.5270/ESA-50a3dd4).

[33] European Space Agency, Technical Assistance for the Deployment of an advanced hyperspectral imaging sensor during SoyFLEX2 (Apr. 2018). [doi:10.5270/ESA-24b3118](https://doi.org/10.5270/ESA-24b3118).

[34] European Space Agency, Photoproxy: Technical Assistance for the Photosynthetic-Proxy Experiment (Nov. 2019). [doi:10.57780/esa-bb0ea39](https://doi.org/10.57780/esa-bb0ea39).

[35] Rascher, Uwe, Siegmann, Bastian, Krieger, Vera, Matveeva, Maria, Quiros, Juan, Muller, Onno, Rademske, Patrick, Herrera, David, Baum, Stephani, Miglietta, Franco, Genesio, Lorenzo, Colombo, Roberto,

Celesti, Marco, Tudoroiu, Marin, Cogliati, Sergio, Carotenuto, Federico, Gioli, Banjamino, Genangelli, Andrea, Hanus, Jan, Houlous, Karel, Migliavacca, Mirco, Martini, David, Martin, M Pilar, Carrara, Arnaud, Moreno, Gerardo, Gonzales-Gascon, Rosario, El-Madany, Tarek, Pacheco-Labrador, Javier, Damm, Alexander, Ahmed, Rifat, Gupana, Remika, Paul-Limoges, Eugenie, Reiter, Ilja, Xueref-Remy, Irène, Mevy, Jean-Philippe, Santonja, Mathieu, Bendig, Juliane, Malenkovsky, Zbynek, Julitta, Tommaso, Burkart, Andreas, FLEX Sentinel Tandem Campaign: Technical Assistance for airborne measurements during the FLEX Sentinel Tandem Experiment (Jul. 2021). [doi:10.57780/esa-ae7953d](https://doi.org/10.57780/esa-ae7953d).

- [36] Rascher, Uwe, Baum, Stephan, Siegmann, Bastian, Buffat, Jim, Burkart, Andreas, Cogliati, Sergio, Colombo, Roberto, Damm, Alexander, Genesio, Lorenzo, Hanus, Jan, Herrera, David, Julitta, Tommaso, Knopf, Oliver, Miglietta, Franco, Muller, Onno, Quiros, Juan, FLEXSense: Technical Assistance for Airborne Measurements during the FLEX Sentinel Tandem Experiment (Mar. 2022). [doi:10.57780/esa-84e5bf5](https://doi.org/10.57780/esa-84e5bf5).
- [37] Rascher, Uwe, Siegmann, Bastian, Baum, Stephan, HyPlant FLEX simulator on SAFIRE ATR42 for LIAISE Experiment (Jul. 2022).
- [38] L. Alonso, L. Gomez-Chova, J. Vila-Frances, J. Amoros-Lopez, L. Gualter, J. Calpe, J. Moreno, Improved Fraunhofer Line Discrimination Method for Vegetation Fluorescence Quantification, IEEE Geoscience and Remote Sensing Letters 5 (4) (2008) 620–624. [doi:10.1109/LGRS.2008.2001180](https://doi.org/10.1109/LGRS.2008.2001180).
- [39] A. Vaswani, N. Shazeer, N. Parmar, J. Uszkoreit, L. Jones, A. N. Gomez, L. Kaiser, I. Polosukhin, Attention Is All You Need (Aug. 2023). [arXiv: 1706.03762](https://arxiv.org/abs/1706.03762), [doi:10.48550/arXiv.1706.03762](https://doi.org/10.48550/arXiv.1706.03762).
- [40] J. Verrelst, J. P. Rivera, C. van der Tol, F. Magnani, G. Mohammed, J. Moreno, Global sensitivity analysis of the SCOPE model: What drives simulated canopy-leaving sun-induced fluorescence?, Remote Sensing of Environment 166 (2015) 8–21. [doi:10.1016/j.rse.2015.06.002](https://doi.org/10.1016/j.rse.2015.06.002).
- [41] P. Gentine, S. H. Alemohammad, Reconstructed Solar-Induced Fluorescence: A Machine Learning Vegetation Product Based on MODIS

Surface Reflectance to Reproduce GOME-2 Solar-Induced Fluorescence, *Geophysical Research Letters* 45 (7) (2018) 3136–3146. [doi:10.1002/2017GL076294](https://doi.org/10.1002/2017GL076294).

- [42] X. Chen, Y. Huang, C. Nie, S. Zhang, G. Wang, S. Chen, Z. Chen, A long-term reconstructed TROPOMI solar-induced fluorescence dataset using machine learning algorithms, *Scientific Data* 9 (1) (2022) 427. [doi:10.1038/s41597-022-01520-1](https://doi.org/10.1038/s41597-022-01520-1).
- [43] P. Yang, C. Van Der Tol, Linking canopy scattering of far-red sun-induced chlorophyll fluorescence with reflectance, *Remote Sensing of Environment* 209 (2018) 456–467. [doi:10.1016/j.rse.2018.02.029](https://doi.org/10.1016/j.rse.2018.02.029).
- [44] P. Yang, C. van der Tol, W. Verhoef, A. Damm, A. Schickling, T. Kraska, O. Muller, U. Rascher, Using reflectance to explain vegetation biochemical and structural effects on sun-induced chlorophyll fluorescence, *Remote Sensing of Environment* (2019). [doi:10.1016/j.rse.2018.11.039](https://doi.org/10.1016/j.rse.2018.11.039).
- [45] F. Pinto, M. Celesti, K. Acebron, G. Alberti, S. Cogliati, R. Colombo, R. Juszczak, S. Matsubara, F. Miglietta, A. Palombo, C. Panigada, S. Pignatti, M. Rossini, K. Sakowska, A. Schickling, D. Schüttemeyer, M. Strózecki, M. Tudoroiu, U. Rascher, Dynamics of sun-induced chlorophyll fluorescence and reflectance to detect stress-induced variations in canopy photosynthesis, *Plant, Cell & Environment* 43 (7) (2020) 1637–1654. [doi:10.1111/pce.13754](https://doi.org/10.1111/pce.13754).
- [46] J. Verrelst, N. Sabater, J. P. Rivera, J. Muñoz-Marí, J. Vicent, G. Camps-Valls, J. Moreno, Emulation of Leaf, Canopy and Atmosphere Radiative Transfer Models for Fast Global Sensitivity Analysis, *Remote Sensing* 8 (8) (2016) 673. [doi:10.3390/rs8080673](https://doi.org/10.3390/rs8080673).
- [47] J. Verrelst, J. P. Rivera Caicedo, J. Muñoz-Marí, G. Camps-Valls, J. Moreno, SCOPE-Based Emulators for Fast Generation of Synthetic Canopy Reflectance and Sun-Induced Fluorescence Spectra, *Remote Sensing* 9 (9) (2017) 927. [doi:10.3390/rs9090927](https://doi.org/10.3390/rs9090927).
- [48] B. D. Bue, D. R. Thompson, S. Deshpande, M. Eastwood, R. O. Green, V. Natrajan, T. Mullen, M. Parente, Neural network radiative transfer

for imaging spectroscopy, *Atmospheric Measurement Techniques* 12 (4) (2019) 2567–2578. [doi:10.5194/amt-12-2567-2019](https://doi.org/10.5194/amt-12-2567-2019).

- [49] AERONET FZJ-JOYCE, AERONET Site Information Database (2024).  
URL [https://aeronet.gsfc.nasa.gov/new\\_web/photo\\_db\\_v3/FZJ-JOYCE.html](https://aeronet.gsfc.nasa.gov/new_web/photo_db_v3/FZJ-JOYCE.html)
- [50] MODIS Atmosphere Science Team, MODIS/Terra Aerosol 5-Min L2 Swath 10km (2017). [doi:10.5067/MODIS/MOD04\\_L2.061](https://doi.org/10.5067/MODIS/MOD04_L2.061).
- [51] MODIS Atmosphere Science Team, MYD04\_L2 MODIS/Aqua Aerosol 5-Min L2 Swath 10km (2017). [doi:10.5067/MODIS/MYD04\\_L2.061](https://doi.org/10.5067/MODIS/MYD04_L2.061).
- [52] Jülich Supercomputing Centre, JURECA: Data centric and booster modules implementing the modular supercomputing architecture at Jülich supercomputing centre, *Journal of large-scale research facilities* 7 (A182) (2021). [doi:10.17815/jlsrf-7-182](https://doi.org/10.17815/jlsrf-7-182).